UNESP – Universidade Estadual Paulista "Júlio de Mesquita Filho"

Instituto de Química de Araraquara

Beatriz Lucas Garrote

The potentiality and limitations of electrochemical impedance spectroscopic methods for molecular film applications

Araraquara

2018

Beatriz Lucas Garrote

The potentiality and limitations of electrochemical impedance spectroscopic methods for molecular film applications

Thesis submitted to post-graduation program from University of São Paulo "Julho de Mesquita Filho" (UNESP, Brazil) in part fulfillment of the requeriment for the degree of Master in Biotechnology.

Supervisor: Prof. Dr. Paulo Roberto Bueno
Co-supervisor: Dr. Flávio Cesar Bedatty

Araraquara
2018

Beatriz Lucas Garrote

Potencial e limitações dos métodos de espectroscópicos de impedância eletroquímica em aplicações para filmes moleculares.

Dissertação apresentada ao Instituto de Química, Universidade Estadual Paulista "Julho de Mesquita Filho" (UNESP) como parte dos requisites para obtenção do título de Mestre em Biotecnologia.

Orientador: Prof. Dr. Paulo Roberto Bueno
Coorientador: Dr. Flávio Cesar Bedatty

Araraquara
2018

FICHA CATALOGRÁFICA

Lucas Garrote, Beatriz
L933p The potentiality and limitations of electrochemical impedance spectroscopy methods for molecular film applications = Potencial e limitações dos métodos de espectroscópicos de impedância eletroquímica em aplicações para filmes moleculares / Beatriz Lucas Garrote. – Araraquara: [s.n.], 2018
75 p.: il.

Dissertação (mestrado) – Universidade Estadual Paulista, Instituto de Química
Orientador: Paulo Roberto Bueno
Coorientador: Flávio Cesar Bedatty

1. Biossensores. 2. Análise eletroquímica. 3. Espectroscopia de impedância. 4. Proteínas. 5. Peptídeos. I. Título

Elaboração: Diretoria Técnica de Biblioteca e Documentação do Instituto de Química de Araraquara
Seção Técnica de Aquisição e Tratamento da Informação

UNIVERSIDADE ESTADUAL PAULISTA

Câmpus de Araraquara

CERTIFICADO DE APROVAÇÃO

TÍTULO DA DISSERTAÇÃO: "The potentiality and limitations of electrochemical impedance spectroscopic methods for molecular film applications"

AUTORA: BEATRIZ LUCAS GARROTE
ORIENTADOR: PAULO ROBERTO BUENO
COORIENTADOR: FLÁVIO CESAR BEDATTY FERNANDES

Aprovada como parte das exigências para obtenção do Título de Mestra em BIOTECNOLOGIA, pela Comissão Examinadora:

Prof. Dr. PAULO ROBERTO BUENO
Departamento de Físico-Química / Instituto de Química - UNESP - Araraquara

Prof. Dr. ASSIS VICENTE BENEDETTI
Departamento de Físico-Química / Instituto de Química - UNESP - Araraquara

Prof. Dr. GERMANO TREMILIOSI FILHO
Departamento de Físico-Quimica / Universidade de São Paulo - USP - São Carlos

Araraquara, 27 de março de 2018

CURRICULUM VITAE

PERSONAL INFORMATION

Name: Beatriz Lucas Garrote

Birth date: 16/09/1993 – Cieza (Murcia) – Spain

Nacionality: Spanish

Professional address: Institute of Chemistry, Univ. Estadual Paulista (UNESP, São Paulo State University). R. Prof. Francisco Degni, 55. Quitandinha – Araraquara – CEP: 14800-900, São Paulo, Brasil.

EDUCATION

- Degree in biotechnology (2011 – 2015). Completed in *Universitat Politécnica de València*, Valencia (Spain).

- Master of biotechnology (2016 – 2018), at *Universidade Estadual Paulista "Júlio de Mesquita Filho"*, Araraquara (São Paulo, Brazil).

INTERSHIP, SCOLARCHIP AND RESEARCH PROJECTS

- Internship in *Centro de Investigación Príncipe Felipe*, Valencia (Spain) (06/2014 – 07/2014) at the Molecular and Cellular Pathology of Alcohol laboratory.

- Scolarship from the Spanish Government. Completed in Chemistry Department of *Universitat Politécnica de València*, Valencia (Spain) (01/2015 – 09/2015) at the Interuniversity Research Institute for Molecular Recognition and Technological Development (IDM). Project: Strategies for the direct detection of specific sequences of genomic DNA in polymeric surfaces.

- Scolarship from FAPESP (São Paulo, Brazil) for Master development. It was completed at the Physical-Chemistry Department of *Universidade Estadual Paulista "Júlio de Mesquita Filho"* at the Nanobionics Group. Project: The potentiality and limitations of electrochemical impedance spectroscopic methods for molecular film applications.

CONFERENCES AND PUBLICATIONS

- IX International workshop on sensors and molecular recognition (2015) in Valencia (Spain).
- LUCAS-GARROTE, B.; MORAIS, S.; MAQUIEIRA, A. Dual signal amplification for highly sensitive hybridization microassays on chemically activated surfaces. **Sensors and Actuators B**: Chemical, v. 246, p. 1108 – 1115, 2017.

A mi madre, Mª Carmen; a mi padre, J. Antonio; a mi hermana, Irene; y a mi hermano, Alejandro.

ACKNOWLEDGEMENTS

I would like to thank my supervisor Prof. Paulo Bueno for the support and the guidance, during these two years.

I would like to acknowledge my co-supervisor Dr. Flávio Bedatty for the support, the scientist discussions and the guidance through the experimental difficulties.

I want to recognize the support and collaboration of my colleagues from Nanobionics, in special Dr. Adriano Santos, Ms. Juliana Cecchetto, Raphael Mazzine and Fernanda Bernardo for the hours spent at the lab, discussing, learning and working together.

I gratefully acknowledge the financial assistance of FAPESP (grant n° 2015/17332-1).

I also would like to thank the Chemistry Institute for the facilities and the administrative personnel from the post-graduation section and from the LIEC.

À minha companheira Gabriela Santos, pelo apoio incondicional, a força, o carinho e o amor. Por me fazer sentir em casa. Esse é só o começo de uma longa viagem.

À minha família brasileira, Isabele e Luisa, por ter ocupado o papel de mãe, pai, irmã e amiga nos momentos que mais precisei.

A mis padres, Mª Carmen y J. Antonio, a mi hermana Irene y a mi hermano Alejandro por haceros sentir tan cerca a 8000 km de distancia.

Abstract

Biomedicine research is directing its effort to achieve fast, simple, point–of–care analytical devices for disease diagnostic. Label-free electrochemical biosensors based on electrochemical impedance spectroscopy (EIS) are an interesting tool for this purpose. For analytical objective, EIS is more sensitive than other electrochemical techniques, such as amperometric, potentiometric or voltammetry. EIS measures the complex resistance of the system. In faradaic EIS system, variations on the electrode surface are monitored by the charge transfer resistance (R_{ct}), so correlations between the variation in R_{ct} value and the concentration of a specific target could be made. Thus, EIS is a widely used technique for biosensing. Here, an EIS based system for the detection of the protein interleukin-6 (IL-6) was proposed. The working electrode was modified with a self-assembled monolayer (SAM) of alkanethiols, in which the biological receptor (Ab IL-6) was covalently immobilized. During the development of the system experimental problems compromised the analytical response. It was analysed every step of the biosensor construction. It was concluded that defects or pinholes on the SAM were the responsible for the absence of response, since EIS is a technique based on charge transfer and the presence of pinholes on the self-assembled monolayer could allow to free ionic and/or electronic migration. Because of this, it was proposed a second system for IL-6 detection based on electrochemical capacitance spectroscopy (ECS) and using a redox peptide SAM. Again, the sensitive of the system was not high enough to the protein detection. According to previous work published by our group, it was possible to correlate the sensitivity of the system with the molecular weight of the biological receptor and the specific target. It was shown that systems with bigger specific target and similar receptors resulted in more sensitive devices. Moreover, it was observed that system with small receptors and bigger targets showed higher sensitivity. IL-6 is a 26 kDa protein and is the smaller protein tested in an ECS based system by our group, and the biological receptor of the system was an antibody (150 kDa), 5.8 times higher than the biological receptor. Thus, the absence of response of the ECS system was attributed to the small molecular weight of the IL-6 protein and the high difference in weight between the biological receptor and the target.

At the same time, it was performed a preliminary electrochemical study of a system with a redox probe confined on the electrode surface and a second one in solution. The objective was study the signal amplifier behaviour observed when two redox probes are

involved on the system and understand the electrochemical process. It was observed the variation from a capacitive-based system, with the confined redox probe, to an impedance one, when the redox probe in solution was present. The presence of two redox probes decreased the redox capacitance of the electroactive film and the resonance resistance of the electrons between the electrode surface and the film; moreover, increased the energy of the system and the frequency of relaxation, due to the increase of the electron diffusion with the solution.

Resumo

A pesquisa em biomedicina está direcionando seus esforços para conseguir desenvolver dispositivos analíticos rápidos, simples e *point-of-care* para o diagnóstico de doenças. Os biossensores eletroquímicos *label-free* baseados na espectroscopia de impedância eletroquímica (EIE) são uma ferramenta interessante para este fim. EIE é uma técnica mais sensível do que outras técnicas eletroquímicas, como as amperométricas, potenciometricas ou voltamétricas. Em um sistema EIE com configuração faradaica, as variações na superfície do eletrodo são monitoradas, geralmente, pela resistência de transferência de carga (R_{ct}) e pode-se correlacionar as variações no valor do R_{ct} com a concentração do analito específico. Assim, EIE é uma técnica muito usada para biossensoriamento. Neste trabalho foi proposto um sistema baseado em EIE para a detecção da proteína interleukina-6 (IL-6). O eletrodo de trabalho foi modificado com uma monocamada auto-organizada (SAM) de alcanotióis. Nela é imobilizado covalentemente o receptor biológico (Ab IL-6). Durante o desenvolvimento do trabalho, foram enfrentados alguns problemas experimentais que comprometeram a resposta analítica do sistema. Para encontrar a causa da falta de resposta, foi analisado cada etapa de construção do biossensor. Após esses estudos foi concluído que as razões da ausência de resposta eram os defeitos ou *pinholes* presentes na SAM, devido ao fato de que EIE é uma técnica baseada na transferência de carga e a presença de defeitos na monocamada pode facilitar a migração iônica e/ou eletrônica. Para resolver isso, foi proposto um segundo sistema para a detecção da proteína IL-6 baseado na ECE (espectroscopia de capacitância eletroquímica), usando uma monocamada auto-organizada formada por um peptídeo redox. De novo, a sensibilidade do sistema não foi suficiente para a detecção da proteína. De acordo com trabalhos publicados previamente pelo nosso grupo de pesquisa, foi possível estabelecer uma correlação entre a sensibilidade do sistema e o peso molecular do antígeno e do receptor biológico. Assim, foi observado que sistemas similares mostram maior sensibilidade quanto maior é o analito. Da mesma forma, foi observado que sistemas com receptores biológicos pequenos e analitos maiores mostram maior sensibilidade. Essas duas afirmações podem ter afetado a sensibilidade do sistema proposto, pois a proteína IL-6 é uma proteína de 26 kDa e é a menor proteína já testada pelo nosso grupo em um sistema ECE e o receptor biológico foi um anticorpo de 150 kDa, 5,8 vezes maior do que o analito. Paralelamente, foi realizado um estudo eletroquímico preliminar de um sistema com duas sondas redox, em solução e confinada

na superfície. O objetivo foi estudar o fenômeno de amplificação de sinal observado quando ambas as sondas redox formam parte do sistema e entender o processo eletroquímico. Foi observada uma transformação de um sistema capacitivo, quando só a sonda redox confinada na superfície está presente para um sistema impedimétrico, quando a sonda redox em solução participa no processo. A presença das duas sondas redox diminuiu a capacitância redox da monocamada eletroativa e a resistência de ressonância e aumentou a energia do sistema e a frequência de relaxação, devido a que foi favorecido a difusão dos elétrons com a solução.

Resumo espandido

Nos últimos anos, o desenvolvimento de metodologias analíticas rápidas e simples para o diagnóstico de doenças tem sido o principal desafio da pesquisa em diagnóstico clínico. Com este objetivo estão sendo usadas duas principais abordagens. Uma delas é baseada no estudo das doenças. As ciências ômicas (genômica, transcriptômica, proteômica ou metabolômica) são uma ferramenta muito utilizada, pois permitem realizar estudos de *screening*, diagnóstico, prognóstico, para o estudo da etiologia de diferentes doenças e para o descobrimento de biomarcadores específicos de uma doença (HORGAN; KENNY, 2011). A segunda abordagem consiste no desenvolvimento de dispositivos analíticos portáteis, fáceis de usar e rápidos que permitam detectar os biomarcadores específicos de uma doença. Esses dispositivos são conhecidos como biossensores. Segundo a IUPAC (MACNAUGHT; WILKINSON, 1997), um biossensor é um instrumento integrado capaz de fornecer uma informação específica quantitativa ou semiquantitativa, usando um elemento de reconhecimento biológico (receptor químico) que está em contato direto com o elemento de transdução.

Dentre todos os tipos de biossensores, aqueles baseados em transdutores eletroquímicos têm sido muito utilizados devido ao baixo custo, à facilidade de uso e a possibilidade de produzir dispositivos pequenos, gerando dispositivos portáteis. Em geral, a configuração dos sistemas eletroquímicos consiste em três eletrodos: o eletrodo de trabalho, em que na sua superfície é imobilizado o receptor biológico; o eletrodo de referência; e o contra eletrodo. Os biossensores eletroquímicos são divididos em função de como é gerado o sinal elétrico. Assim, existem, entre outros, biossensores potenciométricos, que medem variações no potencial de circuito aberto do sistema; biossensores amperométricos, que medem mudanças na corrente do sistema devido à oxidação ou redução de espécies eletroativas na superfície do eletrodo; e biossensores impedimétricos, que medem as mudanças na impedância complexa do sistema (HAMMOND et al., 2016). Desses três, os biossensores impedimétricos podem ser usados em configurações *label-free* e apresentar elevada sensibilidade e baixo custo. Eles são baseados na espectroscopia de impedância eletroquímica (EIE) para monitorar as modificações na superfície do eletrodo de trabalho. É uma técnica usada desde o final dos anos 70, entretanto somente após os anos 2000 foi descoberto o seu potencial como técnica de diagnóstico.

A espectroscopia de impedância mede a resistência elétrica complexa (impedância) da interfase eletrodo-solução, aplicando uma pequena perturbação no potencial a certa frequência e medindo a corrente resultante. O processo é modelado pelo circuito elétrico equivalente de Randles-Ershler. Geralmente, cada modificação do eletrodo de trabalho vai ser monitorada pelo valor do elemento R_{ct} (resistência de transferência de carga) do circuito (DANIELS; POURMAND, 2007; HAMMOND et al., 2016; LISDAT; SCHÄFER, 2008; SANTOS; DAVIS; BUENO, 2014). A EIE é uma técnica muito usada devido a sua sensibilidade. Porém, alguns problemas experimentais que podem comprometer os resultados obtidos têm sido reportados. Bogomolova, et al. (2009) mostraram que a elevada sensibilidade da técnica em sistemas analíticos pode levar a inespecificidade e falsos positivos. Vogt, et al. (2016) reportaram o efeito destrutivo da solução de ferri/ferrocianeto sobre a superfície de ouro depois das medidas e afirmaram que isto poderia comprometer a reprodutibilidade do sistema. Outro elemento importante dos biossensores impedimétricos são as monocamadas auto-montadas ou *self-assembled monolayers* (SAMs),usadas para modificar a superfície do transdutor. As SAMs foram descobertas por Nuzzo e Allara (1983) e consistem em uma camada ordenada de moléculas organizadas de forma espontânea sobre uma superfície sólida, devido às forças intermoleculares (ULMAN, 1996; VERICAT; VELA; SALVAREZZA, 2005). Uma configuração muito usada em sistemas baseados em EIE é a superfície de ouro funcionalizada com moléculas de alcanotióis. Para conseguir uma boa organização sem defeitos as moléculas precisam de 12-16 horas, devem apresentar uma elevada pureza, a superfície deve ser o mais lisa possível e ter o comprimento certo (SIGMA-ALDRICH, 2006). Em sistemas baseados em transferência de carga, como em biossensores impedimétricos, é importante conseguir um bom recobrimento da superfície. Uma monocamada com defeitos ou *pinholes* permitiria a livre migração iônica e eletrônica, não teria o efeito de impedância e a sensibilidade e resposta analítica do sistema se perderia (BOUBOUR; LENNOX, 2000; LEE; LENNOX, 2007).

A capacitância derivada da impedância eletroquímica ou a espectroscopia de capacitância eletroquímica (ECE) pode ser a solução para os problemas experimentais dos sistemas baseados em EIE. ECE mede a capacitância interfacial da monocamada dielétrica do eletrodo e é obtida pela conversão da função da impedância complexa, Z^*, em capacitância complexa, C^*, seguindo a equação (1), onde ω é a frequência angular e *i* é $\sqrt{-1}$ (ORAZEM; TRIBOLLET, 2008).

$$C^*(\omega) = 1/i\omega Z^*(\omega) \quad (1)$$

A capacitância eletroquímica ($C_{\overline{\mu}}$) é o equivalente em escala nano da capacitância química (C_{μ}), quando o eletrodo está imerso em uma solução, como acontece nas medidas de EIS. $C_{\overline{\mu}}$ é resultado da combinação da capacitância iônica (C_i) e da capacitância quântica (C_q). A capacitância iônica ou capacitância da dupla camada (C_{dl}) é a capacitância resultante da camada iônica gerada sobre a superfície do eletrodo. Comparando com um capacitor clássico, a superfície do eletrodo seria uma das placas metálicas e a camada iônica a outra, separadas por nm. Em uma situação não faradaica ou faradaica com a sonda redox em solução (ex. ferroceno), $C_{\overline{\mu}}$ é dominada pela C_i. Quando a sonda redox está confinada na superfície do eletrodo, no potencial formal da monocamada eletroativa, C_q apresenta maior contribuição na $C_{\overline{\mu}}$ do que a C_i, pois C_q depende da densidade de estados da sonda redox da monocamada e da superfície metálica do eletrodo. Em biossensoriamento, as modificações da superfície do eletrodo vão mudar a densidade de estados (Γ) da sonda redox e por tanto a capacitância quântica, enquanto a capacitância iônica (monitorada no potencial redox-out) é quase constante (LEHR et al., 2017). As modificações do sistema vão se monitorar usando a capacitância redox (C_r), seguindo a equação (2), onde *e* é a carga elementar, Γ é a densidade de estados, k_B é a constante de Boltzmann, T é a temperatura absoluta e f é a função de Fermi-Dirac.

$$C_r = \frac{e^2 \cdot \Gamma}{k_B \cdot T} f \cdot (1 - f) \quad (2)$$

Nesse trabalho apresenta-se uma análise crítica de um sistema baseado em EIE. Os problemas experimentais observados durante o desenvolvimento do biossensor foram estudados e analisados com diferentes técnicas para conhecer a causa dos problemas. Os resultados foram comparados com a abordagem baseada em ECE, usando uma monocamada eletroativa de peptídeo. Como prova de conceito, ambos os sistemas foram desenhados para a detecção da proteína interleucina-6 (IL-6). IL-6 é uma

glicoproteína de 26 kDa, que tem um importante papel no processo imune e está envolvida em funções homeostáticas e neuroendócrinas (BARTON, 1997).

Para a construção dos biossensores foi realizado um pré-tratamento da superfície dos eletrodos de ouro. Esse processo consistiu em um polimento mecânico com alumina (1 µm, 0,3 µm e 0,05 µm), voltametria de redissolução em NaOH 0,5 M (100 ciclos desde -1,7 V a -0,7 V a uma velocidade de 100 mV/s) e polimento eletroquímico realizando uma voltametria em H_2SO_4 0,5 M a 80°C (25 ciclos desde -0,2 V a 1,5 V a uma velocidade de 100 mV/s). Os eletrodos limpos foram imersos na solução de monocamada durante 16 horas, sendo MUA + 6-COH 1 mM [1:20] em etanol para os experimentos de EIE e peptídeo redox 2 mM em acetonitrila-agua (1:1 (v/v)) para os experimentos de ECE. Após a formação da monocamada, a SAM foi ativada por 30 minutos com uma solução de EDC 0,4 M e NHS 0,1 M (1:1 (v/v)) para a imobilização do anticorpo. A solução de Ab 1 µM foi preparada em PB pH 7,4 e incubada durante 1 hora. Depois, os grupos não ocupados pelo anticorpo foram bloqueados com BSA 0,1% em PB pH 7,4 durante 30 minutos. A estabilidade do sistema foi testada realizando imersões por 30 minutos em PB pH 7.4. Cada etapa foi caraterizada realizando medidas de CV e EIE. Após a estabilização do sistema foi feito um controle negativo com fetuina (concentração similar à maior concentração de analito usada), e as incubações com o *target* específico. As soluções de proteína foram preparadas em PB pH 7,4 e incubadas durante 30 minutos. Depois foram feitas as medidas de EIE.

Parte experimental configuração EIE O sistema EIE foi otimizado em termos de estabilidade e reprodutibilidade. Porém, não foi obtida uma resposta analítica para nenhuma das proteínas testadas (IL-6, CRP, CEA e HER2). Cada etapa envolvida na obtenção da resposta analítica foi estudada. A atividade analito-anticorpo das proteínas testadas no sistema EIE foi estudada por ELISA. Todos eles mostraram atividade, inclusive nas concentrações usadas no EIE. A imobilização do anticorpo foi verificada por QCM. Após a ativação da SAM, $4{,}3 \cdot 10^{12}$ as moléculas de anticorpo imobilizaram. O anticorpo foi orientado modificando o protocolo, imobilizando a proteína A antes da imobilização do anticorpo e, mesmo assim, não foi obtida uma resposta analítica. Por último foi estudado o efeito da espessura da monocamada na sensibilidade do sistema, substituindo a monocamada de tióis por uma SAM de cisteína e novamente não foi obtida uma resposta analítica. A ultima hipótese proposta foi a presença de *pinholes* na monocamada. O estudo dos defeitos da monocamada foi feito usando o protocolo de

Lee e Lennox (2007) e de Boubour e Lennox (2000). Foi confirmada a presença de defeitos na monocamada, pela imobilização do 11-FcC e pelo ângulo de fase (φ) da medida não faradaica da monocamada. Esses defeitos podem ter sido os responsáveis pela falta de sensibilidade e de resposta analítica do sistema, pois existia livre migração eletrônica e iônica. Para resolver esse problema foi proposto o sistema baseado em ECE.

Parte experimental configuração ECE O sistema ECE usado foi similar ao reportado por Piccoli, et al. (2018). Este sistema consistiu em uma monocamada auto-organizada de um peptídeo redox (Fc-Glu-Ala-Ala-Cys) em que foi imobilizado o anticorpo antiIL-6. A estabilidade obtida e os valores de C_r da SAM e de cada etapa de funcionalização foi muito similar aos obtidos por Piccoli, et al. (2018). O sistema apresentou uma variação de 0,7% entre os três brancos realizados. Porém, apesar da estabilidade, quando foi testado com soluções de diferentes concentrações de proteína IL-6 não foi obtida uma resposta analítica. A IL-6 é a menor proteína testada em um sistema baseado em ECE pelo nosso grupo. Comparando os resultados de trabalhos já publicados pelo grupo é possível correlacionar o tamanho das proteínas e a variação da resposta relativa por década de target (*slope*) das curvas analíticas obtidas para cada proteína e, por tanto à sensibilidade do sistema. Um dos sistemas mais usados consistiu em uma monocamada de 16-MHDA e 11-FcC [1:1]. Ele foi usado para detectar as proteínas NS1 (CECCHETTO et al., 2017), CRP e anti α-sync (FERNANDES et al., 2015), de 46 kDa, 118 kDa e 150 kDa, respetivamente. As curvas analíticas conseguidas apresentaram uma *slope* de 14 para o sistema NS1, 30 para o sistema CRP e 84 para o sistema anti α-sync. A falta de resposta analítica do sistema ECE para a proteína IL-6 pode ser devida ao peso molecular desta proteína não ser suficiente para ser detectada. Além disso, a sensibilidade do sistema também depende da relação do peso molecular entre o receptor biológico e o analito, pois sistemas formados por um receptor biológico menor do que o analito apresentam maior sensibilidade. No sistema do anti α-sync de Fernandes et al. (2015), por exemplo, o receptor foi a α-sync, um receptor celular de 14,4 kDa foi o que apresentou maior sensibilidade. Essa relação também foi reportada por Piccoli, et al. (2018). Eles compararam a sensibilidade do mesmo sistema ECE (monocamada eletroativa de peptídeo) quando era usado um anticorpo como receptor biológico (150 kDa) e um aptámero de DNA. O sistema funcionalizado com o aptâmero mostrou uma sensibilidade quase oito vezes maior do que o sistema com anticorpo. No

sistema para a proteína IL-6 deste trabalho, o receptor biológico foi o anti IL-6, quase seis vezes maior do que a proteína (26 kDa). Assim, a falta de sensibilidade do sistema pode ter sido influenciada pelo pequeno tamanho do analito usado e pela diferença de tamanho entre o receptor e o target.

Parte experimental sistema sonda redox em solução e confinada na superfície: De forma paralela foi estudado o efeito da amplificação de sinal observado no experimento do estudo dos defeitos da SAM, nas medidas faradaicas com sonda redox em solução e imobilizada na superfície. Para isso, três eletrodos foram funcionalizados com o peptídeo redox e foram feitas as medidas de EIE em soluções de diferentes concentrações de $[Fe(CN)_6]^{3-/4-}$ (0,1; 0,2; 0,3; 0,5; 1,0; 2,0 mM). Para entender o processo de transferência de carga, as medidas foram feitas em três potenciais diferentes, no potencial da monocamada eletroativa, 0,38 V; no potencial da sonda redox em solução, 0,22 V e no potencial de meia onda das duas sondas, 0,30 V. Foi analisada a variação de quatro variáveis do sistema: capacitância redox (C_r), frequência de relaxação (k), resistência do sistema (R_q) e o inverso da capacitância redox ($1/C_r$) ou energia do sistema (BUENO; FERNANDES; DAVIS, 2017). A presença das duas sondas redox aumentou a condutividade e a densidade de corrente do sistema. Também, aumentou a energia do sistema e a frequência de relaxação com o aumento da concentração da sonda redox em solução. A capacitância redox do sistema diminuiu, assim como a resistência. Em conclusão, foi observada a transformação de um sistema capacitivo (formado só pela sonda confinada na superfície do eletrodo), em um sistema resistivo na presença da sonda redox em solução. O aumento da condutividade e da densidade de corrente tem concordância com o efeito de amplificação de sinal observado em experimentos anteriores. Esses resultados são promissores e essa configuração pode ser uma boa ferramenta para sistemas muito resistivos ou com baixa sensibilidade.

List of figures

Figure 1 - Biosensor design scheme. 27

Figure 2 – Electrochemical impedance spectroscopy faradaic configuration characteristics. A) Representation of the alkanethiol SAM deposited on the gold electrode surface and the electron transfer between the solution and the electrode surface; B) Nyquist impedance plot; C) Equivalent circuit capable of modeling impedimetric biosensor data; where R_s is the solution resistant; C_m is the monolayer capacitance; R_t the film resistance; C_t the film capacitance; R_{ct} is the redox charge transfer resistant; and Z_w is the Warburg element. The region inside the dashed line corresponds with the non-faradaic system and the continuous line region with the faradaic 29

Figure 3 - Electrochemical capacitance spectroscopy faradaic configuration characteristics. A) Representation of the redox SAM deposited on the gold electrode surface; B) Nyquist capacitance plot; C) Equivalent circuit capable of modeling impedimetric biosensor data; where R_s is the solution resistant; C_m is the monolayer capacitance; R_t the film resistance; C_t the film capacitance; R_{ct} is the redox charge transfer resistant; and C_r is the redox capacitance, used to monitored the modifications of the redox SAM electrode..... 32

Figure 4 - Schematic representation of the electrochemical impedance approach for antigen-antibody interaction. 37

Figure 5 - Nyquist plots of the monolayers tested on gold electrode by different spacer-linker proportion at the formal potential and frequency range 0.1 Hz – 1 MHz. (A) MUA. Active gold electrode area: 0.043 cm^2.; (B) MUA + 6-COH [1:1]. Active gold electrode area: 0.05 cm^2.; (C) [1:5]. Active gold electrode area: 0.042 cm^2.; (D) [1:15]. Active gold electrode area: 0.043 cm^2.; (E) [1:20]. Active gold electrode area: 0.047 cm^2.; (F) [1:30]. Active gold electrode area: 0.04 cm^2..... 40

Figure 6 – Cyclic voltammetry, Nyquist and Bode plots of the electrode functionalization process. A) Cyclic voltamogramm; B) Nyquist impedance plot (-Z'' *vs* Z'); C) Bode plot for real impedance (Z' *vs* frequency); D) Bode plot for imaginary impedance (-Z'' *vs* frequency) of SAM, EDC/NHS, antiIL-6, block and blanks measurements, in the disk gold electrode (from Metrohm), in 1 mM $[Fe(CN)_6]^{3-/4-}$, using 0.5 M KNO_3 and 12 mM PB pH 7.4 as supporting electrolyte. Active gold electrode area: 0.047 cm^2. 42

Figure 7 - Nyquist impedance plot (-Z'' *vs* Z') of 6 blanks measurements (B 1-6): B(1-3) EIS measurement after the first PB pH 7.4 incubation; B(4-6) EIS measurements after 30 min PB pH 7.4 incubation), in the disk gold electrode (from Metrohm), in 1 mM $[Fe(CN)_6]^{3-/4-}$, using 0.5 M KNO_3 and 12 mM PB pH 7.4 as supporting electrolyte. Active gold electrode area: 0.047 cm^2..... 43

Figure 8 - Nyquist and Bode plots of the target recognition steps. A) Nyquist impedance plot (-Z'' *vs* Z'); B) Bode plot for real impedance (Z' *vs* frequency); C) Bode plot for imaginary impedance (-Z'' *vs* frequency) of blanks, negative control with fetuin and IL-6 solutions, in the disk electrode (from Metrohm), in 1 mM $[Fe(CN)_6]^{3-/4-}$, using 0.5 M KNO_3 and 12 mM PB pH 7.4 as supporting electrolyte. Active gold electrode area: 0.047 cm^2..... 44

Figure 9 - Relative variation caused by the blanks incubation and the protein solution for 3 different targets: CRP, HER2 and CEA..... 45

Figure 10 - Characterization of the system construction by QCM. Graphs from top to bottom: EDC/NHS activation; antibody immobilization; and BSA blocking in the quartz crystal. For each procedure, I) signal stabilization with the solution solvent PB (in B and C) or Millipore water (in A); II) incubation with the reagent; III) signal stabilization with the solution solvent..... 47

Figure 11 - Scheme of the distribution of the antibody on the thiolated SAM with and without protein A. A) Direct immobilization: ideal Ab organization when it is directly immobilized by the constant region; B) Direct immobilization: real Ab organization when it is directly immobilized; C) Indirect immobilization: expected organization of the Ab previously protein A immobilization..... 48

Figure 12 - Nyquist and Bode plots of the target recognition steps using an electrode functionalizated with protein A. A) Nyquist impedance plot (-Z'' *vs* Z'); B) Bode plot for real impedance (Z' *vs* frequency); C) Bode plot for imaginary impedance (-Z'' *vs* frequency) of blanks, negative control with fetuin and target solutions, in 1 mM $[Fe(CN)_6]^{3-/4-}$, using 0.5 M KNO_3 and 12 mM PB pH 7.4 as supporting electrolyte. Active gold electrode area: 0.05 cm^2..... 49

Figure 13 - Relative variation caused by the blanks incubation and the protein solutions, using protein A in the system. Target1 = 1 µg mL^{-1}; Target2 = 10 µg mL^{-1}. 49

Figure 14 - QCM results of the cysteine based system. Graphs from top to bottom: Cysteine immobilization; EDC/NHS activation; antibody immobilization; and BSA blocking in the quartz crystal. For each procedure, I) signal stabilization with the solution solvent PB (in A, C and D) or Millipore water (in B); II) incubation with the reagent; III) signal stabilization with the solution solvent. 51

Figure 15 - Nyquist and Bode plots of the target recognition steps using an electrode functionalizated with cysteine monolayer. A) Nyquist impedance plot (-Z'' *vs* Z'); B) Bode plot for real impedance (Z' *vs* frequency); C) Bode plot for imaginary impedance (-Z'' *vs* frequency) of blanks, negative control with fetuin and target solutions, in 1 mM $[Fe(CN)_6]^{3-/4-}$, using 0.5 M KNO_3 and 12 mM PB pH 7.4 as supporting electrolyte. Crystal geometric area: 154 mm^2. 52

Figure 16 - Thiolated SAM distribution on the gold electrode surface. A) Ideal distribution and behaviour of the functionalized electrode; B) hypothetical distribution of the SAM 1:20; C) hypothetical real distribution and deposition of the SAM 1:20 on the gold electrode surface..... 53

Figure 17 - Faradaic and non-faradaic cyclic voltamogramm of the bare gold and the [1:20] SAM in A) 1 mM $[Fe(CN)_6]^{3-/4-}$, using 0.5 M KNO_3 and 12 mM PB pH 7.4 as supporting electrolyte; B) 1 M $NaClO_4$ before and after 5 seconds incubation in 2 mM 11-FcC. Active gold electrode area: 0.05 cm^2. 54

Figure 18 -Nyquist plots of the sequential SAM formation. A) Non-faradaic impedance Nyquist plot; B) Non-faradaic capacitance Nyquist plot of 1 mM 6-COH and 1 mM MUA deposition in 0.5 M KNO_3 and 12 mM PB pH 7.4; C) Faradaic impedance Nyquist plot; D) Faradaic capacitance Nyquist plot of 1 mM 6-COH, 1 mM MUA and 2 mM 11-FcC deposition in 1 mM $[Fe(CN)_6]^{3-/4-}$, using 0.5 M KNO_3 and 12 mM PB pH 7.4. Active gold electrode area: 0.047 cm^2. 55

Figure 19 - Faradaic and non-faradaic cyclic voltamogramm of the bare gold and 6-COH, MUA and 11-FcC deposition, in A) 1 mM $[Fe(CN)_6]^{3-/4-}$, using 0.5 M KNO_3 and 12 mM PB pH 7.4 as supporting electrolyte; B) 0.5 M KNO_3 and 12 mM PB pH 7.4; C) 1 M $NaClO_4$ after and before 60s and 300s incubation with 2 mM 11-FcC solution. Active gold electrode area: 0.047 cm^2. 56

Figure 20 - Study of the the phase angle (***φ***) of the SAM constructed in sequential as an analyses of the presence of pinholes. 57

Figure 21 - Redox peptide SAM stability. M1-9: nine consecutive EIS measurements of the electroactive film. Active gold electrode area: 0.045 cm^2. 59

Figure 22 – Cyclic voltammogram, Nyquist and Bode plots of the ECS based electrode functionalization process. A) Cyclic voltammogram; B) Nyquist capacitance plot (-C'' *vs* C'); C) Bode plot for real capacitance (C' *vs* frequency); D) Bode plot for imaginary capacitance (-C'' *vs* frequency) of SAM, SAM at de redox-out potential, antiIL-6, block and blanks measurements in 20 mM TBA as supporting electrolyte. Active gold electrode area: 0.045 cm^2. 60

Figure 23 - Study of the stability of the biosensor surface for the protein IL-6. B1-3: triplicate EIS measurements after 30 min immersion in PB. B4-6: triplicate EIS measurements after a second immersion in PB during 30 min. B7-9: triplicate EIS measurements a third immersion in PB for 30 min. Active gold electrode area: 0.045 cm^2. 61

Figure 24 - Nyquist and Bode plots of the detection of the protein IL-6. A) Nyquist capacitance plot (-C'' *vs* C'); B) Bode plot for real capacitance (C' *vs* frequency); C) Bode plot for imaginary capacitance (-C'' *vs* frequency) in 20 mM TBA as supporting electrolyte. Active gold electrode area: 0.045 cm^2. 61

Figure 25 - Nyquist impedance plot of the detection of the protein CRP from Piccoli, et al. 62

Figure 26 - Cyclic voltammetry plots of redox peptide SAM and redox probe in solution. A) CV in $[Fe(CN)_6]^{3-/4-}$ in 0.5 M KNO_3 and 12 mM PB, comparing to B) cyclic voltammetry of redox peptide-based SAM in 20 mM TBA; 20 mM TBA and 0.1 mM $[Fe(CN)_6]^{3-/4-}$; and in 20 mM TBA after the measurements. In A) vertical reference

represents the formal potential of the $[Fe(CN)_6]^{3-/4-}$ in 0.5 M KNO_3 and 12 mM PB, 0.25 V (dotted line); in B) the vertical references show the formal potential of the confined redox probe (redox peptide SAM), 0.38 V *versus* Ag|AgCl 3M KCl (dashed line); of the redox probe in 20 mM TBA, 0.22 V *versus* Ag|AgCl 3M KCl (dotted line); and the half potential of both redox probe, 0.30 V *versus* Ag|AgCl 3M KCl (dash-dot line). Active gold electrode area: 0.045 cm^2..... 64

Figure 27 - EIS measurement in 0.38 V *versus* Ag|AgCl 3M KCl of the redox peptide SAM and redox probe in solution. A) Impedance Nyquist impedance plot; B) Capacitance Nyquist plot; C) Bode plot of real impedance (Z'); D) Bode plot of imaginary impedance (Z''); E) Bode plot of real capacitance (C'); F) Bode plot of imaginary capacitance (C''). Active gold electrode area: 0.045 cm^2..... 65

Figure 28 - EIS measurement in 0.30 V *versus* Ag|AgCl 3M KCl of the redox peptide SAM and redox probe in solution. A) Impedance Nyquist impedance plot; B) Capacitance Nyquist plot; C) Bode plot of real impedance (Z'); D) Bode plot of imaginary impedance (Z''); E) Bode plot of real capacitance (C'); F) Bode plot of imaginary capacitance (C''). Active gold electrode area: 0.045 cm^2..... 66

Figure 29 - EIS measurement in 0.22 V *versus* Ag|AgCl 3M KCl of the redox peptide SAM and redox probe in solution. A) Impedance Nyquist impedance plot; B) Capacitance Nyquist plot; C) Bode plot of real impedance (Z'); D) Bode plot of imaginary impedance (Z''); E) Bode plot of real capacitance (C'); F) Bode plot of imaginary capacitance (C''). Active gold electrode area: 0.045 cm^2..... 67

Figure 30 - Analysis of the variation of the variables involved on the charge transfer process of the system with both redox probe confined and in solution. A) Redox capacitance, C_r; B) Inverse of the redox capacitance, $1/C_r$; C) Resonance resistance, R_q; D) Frequency of charge relaxation, k. For each plot: black= EIS measurements in 0.38 V; red= EIS measurements in 0.30 V; green= EIS measurements in 0.22 V..... 68

List of tables

Table 1 - R_{ct} values, stability and reproducibility of the different SAMs tested. 39

Table 2 - ELISA assay results. Absorbance values of the proteins tested. 45

Table 3 - Variation values in % of the blanks and the proteins measurements in different proteins..... 45

Table 4 - Absolute frequency variation, mass variation and number of molecules per cm^{-2} of the QCM assay for the cysteine, antibody and BSA immobilization. 52

Table 5 - Correlation coefficients (r^2) of the lineal regression showed in Figure 29 for each variable and each potential. 69

List of abbreviations and symbols

11-FcC	11-ferrocenylundecacethiol
6-COH	6-mercapto-1-hexanol
Ab	Antibody
Ala	Alanine
anti-	Antibody
BSA	Bovine serum albumin
c	Theoretical QCM sensitivity coefficient
C'	Real componente of complex capacitance
C''	Imaginary componente of complex capacitance
C^*	Complex capacitance
$C_{\overline{\mu}}$	Electrochemical capacitance
C_{dl}	Double layer capacitance
C_e	Electrostatic capacitance
CEA	Carcinoembryonic antigen
C_m	Monolayer capacitance
C_q	Quantum capacitance
C_r	Redox capacitance
CRP	C-reactive protein
C_t	Target capacitance
CV	Cyclic voltammetry
Cys	Cysteine
e	Elementary charge
ECE	Espectroscopia de capacitância eletroquímica
ECS	Electrochemical capacitance spectroscopy
EDC	1-Ethyl-3-(3-dimethylaminopropyl) carbodiimide (EDC)

EIE	Espectroscopia de impedância eletroquímica
EIS	Electrochemical impedance spectroscopy
ELISA	Enzyme linked inmunosorbent assay
Eq.	Equation
f	Fermi-Dirac function
F_{ab}	Variable region of an antibody
F_c	Constant region of an antibody
Fc	Ferrocenyl
FRA	Frequency response analysis
Glu	Glutamic acid
HER2	Human epidermal growth factor receptor 2
hPAP	Human prostatic acid phosphatase
HRP	Horseradish peroxidase
i	$\sqrt{-1}$
IgG	Immunoglobulin G
IL-6	Interleukin-6
φ	Phase angle
k	Frequency
k_B	Boltzman constant
LOD	Limit of detection
M_m	Molecular mass
MUA	11-mercaptoundecanoic acid
N_A	Avogadro's constant
NHS	N-Hydrosuccinimide
NS1	Non-structural protein 1
OPD	o-Phenylenediamine dihydrochloride
PB	Phosphate buffer

PBS-T	Phosphate buffered saline with Tween 20
PEG	Polyethylene glycol
QCM	Quartz crystal microbalance
r^2	Coefficient of regression
R_{ct}	Charge transfer resistance
R_q	Quantum resistance
R_s	Solution resistance
RSD	Relative standard desviation
R_t	Target resistance
SAM	Self-assembled monolayer
T	Absolute temperature
TBA	tetrabutylammonium bromide
ω	Angular frequency
Z'	Real component of the complex impedance
-Z"	Imaginary component of the complex impedance
Z^*	Complex impedance
Z_w	Warburg element
α-sync	α-synuclein
Γ	Density-of-states
Δm	Mass variation
ΔE_p	Different between oxidation and reduction potential
Δf	Frequency variation

Summary

1. Introduction 27
1.1. Electrochemical impedance spectroscopy (EIS) 28
1.2. Electrochemical capacitance spectroscopy (ECS) 31
2. Objective 34
3. Experimental 34
3.1. Material, reagents and apparatus 34
3.2. Electrode surface pre-treatment 35
3.3. Electrochemical measurements 35
3.4. Gold electrode functionalization 36
3.5. Antigen-antibody interaction 37
3.6. Enzyme Linked Immunosorbent Assay (ELISA) 37
3.7. Quartz Crystal Microbalance (QCM) assays. 38
4. Results and discussions 39
4.1. Self-assembled monolayer optimization. 39
4.2. Faradaic electrochemical impedance spectroscopy assay. 40
4.3. Study of the pair antigen-antibody activity. 44
4.4. Study of the antibody immobilization step. 46
4.5. Oriented-Ab-immobilization with protein A. 48
4.6. Simultaneous QCM and EIS assay with cysteine monolayer. 50
4.7. Study of the MUA + 6-COH 1:20 self-assembled monolayer defects. 53
4.8. Faradaic impedance-derived capacitance assay. 58
4.9. Electrochemical analysis of an electroactive film based system with redox probe in solution. 63
5. Conclusion 72
References 73

1. Introduction

In the last decades, the development of fast and simple analytical methods for disease diagnostic is one of the principal challenges for clinical research. In this direction, two principal approaches are being developed. One of them is based on the diseases study. Omic sciences (genomics, transcriptomics, proteomics or metabolomics) have transformed the way to study cellular and molecular systems, becoming an important tool for screening, diagnosis, prognosis or understanding the aetiology of the diseases. Such strategy lend to discovery biomarkers of the disease (HORGAN; KENNY, 2011) ("characteristic that is objectively measured and evaluated as an indicator of normal biological processes, pathogenic processes, or pharmacologic responses to a therapeutic intervention", according to the National Institutes of Health Biomarkers Definitions Working Group in 1998 (ATKINSON et al., 2001)). The second approach is the development of portable, nice handle and rapid analytical devices suitable for biomarker detection in the field. These devices, called biosensors, are a self-contained integrated which are capable of providing specific quantitative or semiquantitative analytical information using a biological recognition element (biochemical receptor) which is in direct spatial contact with a transduction element, according to IUPAC (MACNAUGHT; WILKINSON, 1997) (Figure 1).

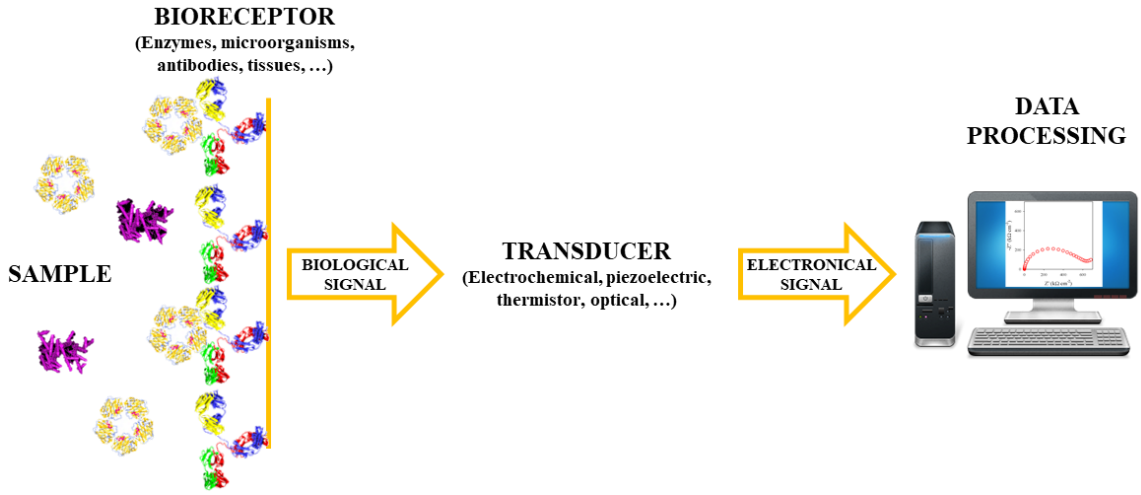

Figure 1 - Biosensor design scheme.

Source: Author

Among different biosensors, those based on electrochemical transducers (the biorecognition generates an electrical signal) are widely used, because they are low-cost and easy-to-use; and they can be miniaturized and portable, essential characteristics of biosensors. In general, those biosensors are constituted by a three-electrode system: a working or sensing electrode, whose

surfaces is modified with the bioreceptor; a reference electrode; and a counter electrode (HAMMOND et al., 2016). Electrochemical biosensor are divided according to how is generated the electrical signal. Some examples are potentiometric, amperometric or impedimetric.

Potentiometric biosensors usually measure variations in the open circuit potential of the system. The first potentiometric biosensor was described in 1969 by Guilbault and Montalvo (1969). It was an enzyme biosensor for the detection of urea in body fluids. It was based on the immobilization of the enzyme urease on an ammonia electrode. In the presence of urea, the enzyme catalysed its decomposition to ammonium ion, detectable by the ammonia electrode. Although potentiometric is an inexpensive, well-known technique, it shows worse analytical characteristics than using an amperometric transducer (KONCKI, 2007). Amperometric biosersors measure changes in current due to the oxidation or reduction of species on the electrode surface. Clark and Lyons (1962) developed the first amperometric-enzyme biosensor for glucose determination. Since then, numerous strategies have been published, most of them label-based. For analytical purpose, both methodologies require a tag, as a secondary antibody, an enzyme or a redox label (SANTOS; DAVIS; BUENO, 2014). Label-based configurations show disadvantages comparing with label-free techniques, since they need additional steps due to the process of labelling, so they are more laborious and time-consuming strategies. Label-free configurations bypass the label step, reduces the experimental time required and determine interactions in real-time (RAY; MEHTA; SRIVASTAVA, 2010). Potentiometric and amperometric transducers do not present the selectivity and sensitivity required by a label-free system. On the other hand, impedimetric biosensors have the potential for a label-free detection with highly sensitivity and low cost.

1.1. Electrochemical impedance spectroscopy (EIS)

It measures the system complex impedance (Z^*) in every electrode surface modification. These biosensors use electrochemical impedance spectroscopy (EIS) to monitor each immobilization event on the electrode surface. This technique has been used since late 1970s in corrosion studies, battery construction and in studies about charge transport across membranes. Its potential in diagnostics was discovered in the 2000s (DANIELS; POURMAND, 2007; LISDAT; SCHÄFER, 2008; ORAZEM; TRIBOLLET, 2008). Since then, more than 2000 works have been published, according with Pubmed. Most of them are based on a faradaic configuration with redox probe in solution (Figure 2A). EIS measures the complex electrical resistance (impedance) of the electrode-solution interface by applying a

small sinusoidal voltage at certain (and controllably varied) frequency and measuring the resulting current. Figure 2B shows the typical Nyquist impedance plot obtained. The process can be modeled by the Randles-Ershler electrical equivalent circuit (Figure 2C) and the R_{ct} element (charge transfer resistance) is used for monitor the surface modifications, since each variation of the surface changes the electron transfer process between the redox probe in solution and the electrode surface. Thus, R_{ct} value changes proportionally to the target concentration, achieving a high sensitivity (it have been reported limit of detection (LOD) in order of pg mL^{-1}) (BAHADIR; SEZGINTÜRK, 2016; SANTOS; DAVIS; BUENO, 2014).

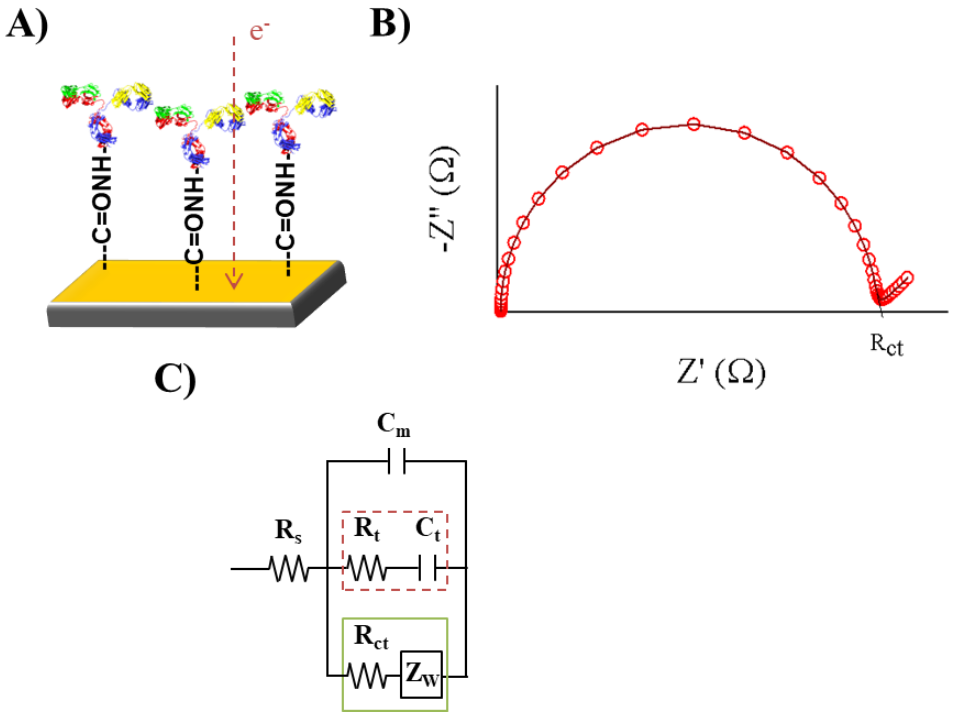

Figure 2 – Electrochemical impedance spectroscopy faradaic configuration characteristics. A) Representation of the alkanethiol SAM deposited on the gold electrode surface and the electron transfer between the solution and the electrode surface; B) Nyquist impedance plot; C) Equivalent circuit capable of modeling impedimetric biosensor data; where R_s is the solution resistant; C_m is the monolayer capacitance; R_t the film resistance; C_t the film capacitance; R_{ct} is the redox charge transfer resistant; and Z_w is the Warburg element. The region inside the dashed line corresponds with the non-faradaic system and the continuous line region with the faradaic.
Source: Author

In our group, some work have been published showing the potential of EIS in biosensing (CECCHETTO et al., 2015; FERNANDES et al., 2014) Both consisted in an immunosensor (antibody as a bioreceptor), faradaic system with redox probe (potassium ferri/ferrocyanide) in solution. Cecchetto, et al. (2015) developed a system based in an alkanethiol SAM for NS1 detection. They achieved a sensitivity of 14.1 percentage of variation per decade of protein (LOD of 3 ng mL^{-1}). Fernandes, et al. (FERNANDES et al., 2014) reported an EIS system for

the detection of the protein CRP, achieving a limit of detection (LOD) of 0.264 nmol L^{-1}. Although EIS has been proved to be an interesting technique for biosensing, it shows some experimental problems, as it is presented in this report. Sensitivity is the principal reason that makes EIS so popular. However, it can be a drawback, as was reported by Bogomolova et al. (2009) high sensitivity can be correlated with unspecific or false positive response. They described some factors that can change impedance without specific receptor – target interaction, such as initial electrode contamination (non-cleaned surface), repetitive EIS or CV measurements or immersions in the measurements buffer between measurements. Another drawback of the faradaic EIS system is the surface destruction by the $[Fe(CN)_6]^{3-/4-}$ solution. Vogt et al. (2016) reported that measurements in ferri/ferrocyanide solution damage the electrode surface by the free CN^- ions. Thus, after each measurement the surface changes and reproducible EIS measurements are not possible, even at the bare gold. This would be in agreement with the Bogomolova et al. observations. Notice that it was difficult to find references at the literature about the experimental difficulties. Those problems could compromise the reproducibility and sensitivity of the EIS based systems.

Commonly, in impedimetric biosensors the transducer surface is modified by a self-assembled monolayer (SAM) of alkanethiols, where is immobilised the specific biological receptor of the target of interest, usually an antibody. Self-assembled monolayers (SAMs) are organized single-molecule-thick films, based on a group of molecules spontaneously immobilized in an ordered and oriented way in a solid surface by intermolecular forces (ULMAN, 1996; VERICAT; VELA; SALVAREZZA, 2005). Since it was discovered by Nuzzo and Allara in 1983 (1983) that alkanethiols molecules had the ability to autoassembled spostaneously on noble metal surfaces, it constituted a versatile tool for creating surfaces with different chemical characteristic, since the head functional groups of the alkanethiols can be modified, thus the chemical properties of the SAM, enabling interactions with adjacent molecules or analytes. Those properties made SAMs an interesting element for biosensing. Alkanethiols have shown the ability to assembled on metal (Au, Pt, etc.), semiconductors or in oxide surfaces (SMITH; LEWIS; WEISS, 2004). In impedimetric biosensor it is widely used gold surfaces. The self-assembled of alkanethiols on a gold surface is governed by the combination of two driving forces. The first is the affinity that the sulphur groups present for gold, creating a stable and semi-covalent bond. The second driving forces are the van der Waals interactions between the methylene groups from the alkanethiols structures. The molecules immobilization and surface coverage is a very fast process, in the order of seconds or minutes. However, the monolayer requires more time (from 12 hours to 2 days) to get ordered and decrease the

uncovered defects (SIGMA-ALDRICH, 2006). Those defects can be caused by the purity of the alkanethiol used, the surface roughness and the length of the molecules. As was reported by Lee and Lennox, coverage defects in thiol-based SAMs are an important issue in system based on electron transfer process with redox probe in solution, such as EIS systems, where the electronic and ionic migration would be possible and the insulating properties of the SAM would be compromised (BOUBOUR; LENNOX, 2000; LEE; LENNOX, 2007). Those experimental issues were observed and studied in this work.

1.2. Electrochemical capacitance spectroscopy (ECS)

As was mentioned above, impedimetric biosensor could show some experimental problems that could compromised the reproducibility and sensitivity of the system. Thus, EIS could not be the best technique for biosensing. Here is proposed the impedance-derived capacitance or electrochemical capacitance spectroscopy (ECS) approach as a better alternative. ECS measures the interfacial capacitance of the electrode dielectric monolayer and is calculated by C^* obtained by conversion the impedance complex function Z^*(composed of real, Z', and imaginary, Z'', components) from the EIS measurement, using the Eq. (1), wherein ω is the angular frequency and i is $\sqrt{-1}$ (ORAZEM; TRIBOLLET, 2008)

$$C^*(\omega) = 1/i\omega Z^*(\omega) \quad (1)$$

The electrochemical capacitance ($C_{\overline{\mu}}$) is the nanoscale equivalent of the chemical capacitance (C_μ) when the electrode is embedded into an electrolyte, such as in the EIS measurements. $C_{\overline{\mu}}$ is constituted by the combination of the ionic capacitance (C_i) and the quantum capacitance (C_q), following the Eq. (2). The ionic capacitance or double layer capacitance (C_{dl}) is the resultant capacitance of the ion layer generated on the electrode surface, so, comparing with a classic capacitor, the electrode surface is one metallic plate and the ion layer is the other, separated by nm. In a non-faradaic situation or faradaic with redox probe in solution, $C_{\overline{\mu}}$ would be governed by the ionic capacitance. When the redox probe is confined on the electrode surface, a *pseudo-capacitance* is observed. In this case, at the formal potential the quantum capacitance has a higher contribution in the $C_{\overline{\mu}}$ value than the C_i, since C_q depends on the density-of-states of the confined redox probe and the metallic electrode surface.

$$\frac{1}{C_{\bar{\mu}}} = \frac{1}{C_i} + \frac{1}{C_q} \quad (2)$$

For biosensing, the electrodes modifications alter the density-of-state (Γ) of the redox probe, and so the C_q value, while the C_i value (monitored at the redox-out potential) would be almost constant (LEHR et al., 2017). Surface modifications are monitored by the redox capacitance (C_r), following the Eq. (3), wherein *e* is the elementary charge, Γ is the density-of-states, k_B is the Boltzmann constant, T is the absolute temperature and f is the Fermi Dirac function. C_r would be maximized when $f = 1/2$ (half of the available sites are occupied and half do not). This occurs at the half wave potential of the system, at which the measurements are performed. Experimentally, C_r corresponds with the diameter of the semicircle obtained after the measurement (Figure 3B). It is modeled by a derived Randles-Ershler circuit, showed in Figure 3C.

$$C_r = \frac{e^2 \cdot \Gamma}{k_B \cdot T} f \cdot (1 - f) \quad (3)$$

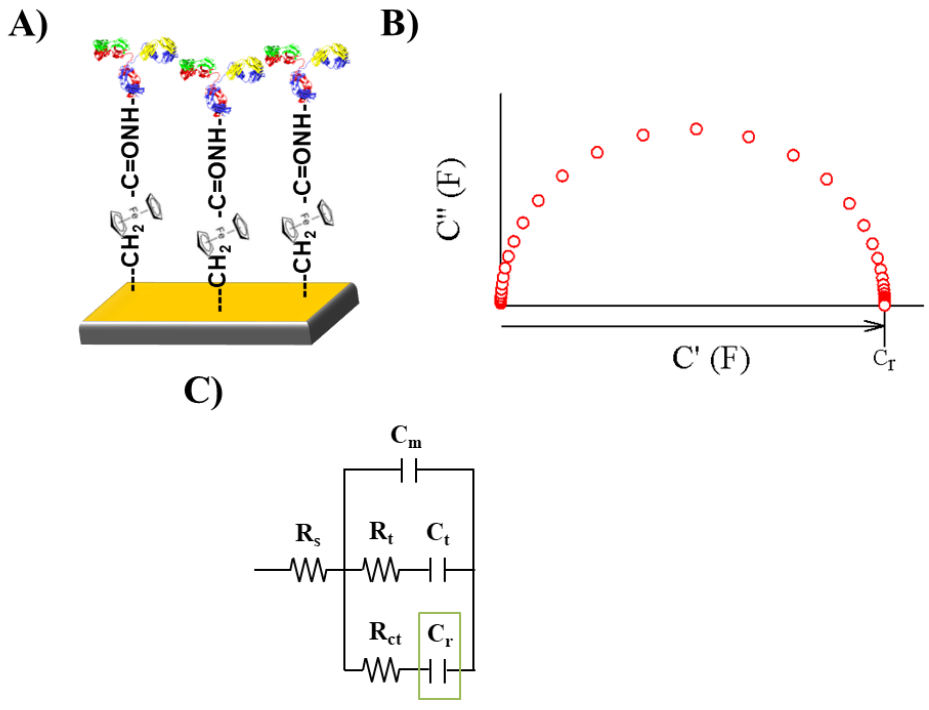

Figure 3 - Electrochemical capacitance spectroscopy faradaic configuration characteristics. A) Representation of the redox SAM deposited on the gold electrode surface; B) Nyquist capacitance plot; C) Equivalent circuit capable of modeling impedimetric biosensor data; where R_s is the solution resistant; C_m is the monolayer capacitance; R_t the film resistance; C_t the film capacitance; R_{ct} is the redox charge transfer resistant; and C_r is the redox capacitance, used to monitored the modifications of the redox SAM electrode.

Source: Author

The potential of ECS in biosensing have been widely studied and proved by our group. Fernandes, et al. developed a ECS-based biosensor for α-sync and CRP, using a thiolated redox SAM with 11-ferrocenyl-undecanethiol (11-FcC) (FERNANDES et al., 2015). Cecchetto, et al. applied the same system as that reported by Fernandes, et al. (2015) for NS1 detection and compared it with the EIS configuration. They showed a limit of detection (LOD) 15 times lower using the ECS configuration instead of the EIS (CECCHETTO et al., 2017). The protein hPAP (human prostatic acid phosphatase) was also detected, using an ECS system by Fernandes, et al. (2017). They used a SAM composed by PEG (polyethylene glycol) and 11-FcC [1:99] and achieved a LOD of 4.1 ± 1.3 pM. That same self-assembled monolayer was used by Santos, et al. (2018) for the detection of two biomarkers for dengue diagnostic (NS1 and IgG levels). The achieved sensitivities (percentage of signal variation per decade of protein concentration) were 4.5 for NS1 and 6.3 for IgG. Other redox surfaces non-based on 11-FcC were tested too. Redox peptide-based electroactive SAMs show advantages over redox alkanothiolated SAMs, such as peptide are easily manipulated and they can be designed to be the receptor of specific target (AMBLARD et al., 2006). Santos, et al. used an electroactive peptide SAM for CRP detection, showing a limit of detection of 94 ng mL^{-1} (SANTOS et al., 2015). The capacity of self-assembled and its utility in ECS system were tested with different peptides, as was reported by Piccoli, et al. (2016).

Here, a critical analysis for the EIS approach is presented. A mix thiol-based self-assembled monolayer was chemisorbed on the electrode surface for protein detection by EIS. The experimental problems observed during this objetive were deeply studied using different techniques, such as QCM and ELISA, and by faradaic and non-faradaic strategies. Those result were compared with the faradaic ECS approach, using an electroactive peptide based SAM, in terms of sensitivity and reproducibility. As a proof of concepts, the systems (both EIS and ECS configuration) were designed for the detection of the protein interleukin 6 (IL-6). Human IL-6 is a 26 kDa glycoprotein, member of the cytokines family. It has an important role in immune process and it is involved in homeostatic and neuroendocrine functions (BARTON, 1997).

2. Objective

The main objective of this work was the study of the potentials and limitations of the electrochemical impedance spectroscopy methods for analytical purpose. Thus, the short-term objectives were:

- Study of the interaction event.
- Study of the bioreceptor immobilization event.
- Study of the bioreceptor orientation.
- Study of the presence of pinholes on the self-assembled monolayer.

The second objective was to achieve a responsive ECS based system for protein IL-6 detection, using an electroactive redox-peptide based SAM.

3. Experimental

3.1. Material, reagents and apparatus

Sodium hydroxide, potassium hydroxide, 1-Ethyl-3-(3-dimethylaminopropyl) carbodiimide (EDC), N-Hydrosuccinimide (NHS), sodium chloride, trisodium citrate dihydrate, monopotassium phosphate, sodium phosphate dibasic dodecahydrate, potassium chloride, sodium carbonate, sodium bicarbonate, sodium nitrate, tetrabutylammonium bromide (TBA), potassium ferricyanide and potassium ferrocyanide were purchased from Sigma-Aldrich. The thiols 11-mercaptoundecanoic acid (MUA) and 6-mercapto-1-hexanol (6-COH) for monolayer construction were purchased from Sigma-Aldrich. Antibodies (Ab) for HER2 (Human epidermal growth factor receptor 2), CRP (C-reactive protein) and CEA (Carcinoembryonic antigen) were purchased from Sigma-Aldrich. Antibody and IL-6 protein were purchased from Rhea Biotech.

The buffer solutions used were: 12 mM Phosphate buffer (PB pH 7.4: 0.27 g L^{-1} monopotassium phosphate, 3.58 g L^{-1} sodium phosphate dibasic dodecahydrate); 1 mM $[Fe(CN)_6]^{3-/4-}$ in 0.5 M KNO_3 in 12 mM PB pH 7.4 (1 mM potassium ferricyanide, 1 mM potassium ferrocyanide); carbonate/bicarbonate buffer pH 9 (1.59 g L^{-1} sodium carbonate, 2.39 g L^{-1} sodium bicarbonate); PBS-T (8 g L^{-1} sodium chloride; 0.2 g L^{-1} monopotassium phosphate; 1.15 g L^{-1} sodium phosphate dibasic dodecahydrate; 0.2 g L^{-1} potassium chloride; 0.2 g L^{-1} sodium nitrate; 0.5% tween 20).

3.2. Electrode surface pre-treatment

The state of the gold surface affects the monolayer formation and therefore the measurements, so it is necessary a pre-treatment protocol. It started with mechanical polishing steps with a grinding machine, from Dremel, and aluminum oxide pads (1 µm, 0.3 µm and 0.05 µm), from Buheler. Then, the electrode was sonicated in water 2 min between the polishing steps to remove the aluminum particles adhered to the surface. After that, it was carried out the electrochemical polished in 0.5 M NaOH solution (100 cycles from -1.7 V to -0.7 V at a scan rate of 100 mV/s) and subsequently in 0.5 M H_2SO_4 solution at 80°C (50 scans from -0.2 V to 1.5 V at a scan rate of 100 mV/s). The cathodic peak area from the 0.5 M H_2SO_4 voltammogram depends on the quality of the active gold surface. Using a conversion factor of 410 µC cm^{-2} (TRASATTI; PETRII, 1991) the active gold area can be obtained. The ratio between this area and the geometrical area of the electrode (0.03142 cm^2) is the active surface roughness. This is the factor to evaluate the electrode quality for experiments. The active surface roughness value will be kept lower than 1.50 for reproducible results. The fresh polished surface was characterized by cyclic voltammetry (CV) and electrochemical impedance spectroscopy (EIS) in 1 mM $[Fe(CN)_6]^{3-/4-}$ in 0.5 M KNO_3 in 12 mM PB pH 7.4 (section 3.3.) to evaluate the electrode surface state. Thereafter, CV in 0.5 M H_2SO_4 solution at 80°C was performed before electrode modification.

3.3. Electrochemical measurements

Electrochemical measurements were performed in an Autolab Potentiostat equipped with a frequency response analysis (FRA) module using a three-electrode system: a gold disk working electrode (2.0 mm diameter from Metrohm) with a platinum wire counter electrode and a silver/silver chloride (Ag/AgCl, filled with 3.0 M KCl) reference electrode. *All potentials reported are relative to this reference electrode*. The results were treated with the programs NOVA 11.0 and Sigma Plot 11.0.

The systems were characterized by two types of measurements, cyclic voltammetry (CV; -0.2 V to 0.7 V at a scan rate of 100 mV s^{-1}) and electrochemical impedance spectroscopy (EIS; frequency range from 100 mHz - 1 MHz with a peak-to-peak amplitude of 20 mV and at the formal potential; each measurement was performed in triplicate). In the impedimetric system, the measurements were performed with the redox probe in solution (Figure 2), using 1 mM $[Fe(CN)_6]^{3-/4-}$ in 0.5 M KNO_3 in 12 mM PB pH 7.4 as a supporting electrolyte at the formal potential of the redox probe in solution. In the capacitive system the redox probe was

confined on the surface (electroactive films; Figure 3). The measurements were performed in 20 mM $TBAClO_4$ in acetonitrile and water (1:4 (v/v)) at the formal potential of the electroactive film (calculated by CV). The capacitance results were obtained by the conversion of the impedance function (Z^*) to capacitance complex function (C^*), using the Eq. (1).

In the systems with the redox probe in solution, the surface modifications were monitored by the charge transfer resistance (R_{ct}), fitting with the Randles-Ershler equivalent circuit (Figure 2). In the systems based on electroactive films, surface changes would be monitored by the redox capacitance (C_r) (Figure 3), which depends on the density-of-states of the confined redox probe, given by Eq. (3).

3.4. Gold electrode functionalization

Fig. 3 shows a scheme of the process. A freshly cleaned disk gold electrode (mechanically and electrochemically polished; section 3.2.) was immersed for 16h at room temperature in the self-assembled monolayer solution (1 mM MUA + 6-COH [1:20] in ethanol for the impedance-based experiments and 2 mM redox peptide in acetonitrile and water (1:1 (v/v)) for the capacitive-based experiments). It was cleaned with ethanol or acetonitrile – water solutions (depend on the SAM type), dried with nitrogen and characterized by CV and EIS. SAM stability was analysed immersing the electrode in PB pH 7.4 for 30 min and then characterizing by EIS. The SAM modified gold electrode was immersed in the 0.4 M EDC (500 µL) and 0.1 M NHS (500 µL) aqueous solution for 30 min and then incubated for 1h with the antibody (Ab) solution (1 µM) in PB pH 7.4. The electrode was cleaned with PB pH 7.4, distilled water, dried under nitrogen and characterized. The unbound carboxylic groups were blocked with 0.1% BSA solution in PB pH 7.4 for 30 min. Thereafter the surface was cleaned and characterized as stated before. For study the system stability, the functionalized disk electrode was immersed in PB pH 7.4 for 30 min, and then characterized by EIS. It was repeated twice. After that, a negative control was performed, incubating 30 min the functionalized electrode with a concentration of fetuin similar as the highest target concentration used. Then, it was cleaned and characterized. After the negative control, a new blank measurement was performed (immersion in PB pH 7.4 for 30 min) and, again, it was cleaned and characterized.

Any protocol changes will be reported and discussed in the result section (section 4).

3.5. Antigen-antibody interaction

The stable-functionalized electrode (section 3.4.) was then incubated with the target solutions. Figure 4 shows a scheme of the process. Each target solution prepared in PB pH 7.4 was incubated for 30 min, and then the electrode was cleaned with PB, distilled water, dried with nitrogen and characterized by EIS (section 3.3.). After the measurement, the electrode was cleaned with distilled water, PB, dried with nitrogen and incubated with the next target solution. This procedure was repeated for all the protein solutions from the smallest concentration to the highest one. The antibody – target interactions causes a detectable, measurable and quantifiable change in EIS measurements, so a correlation would be achieved. Each EIS measurement was done three times (triplicate) to obtain average and standard deviation (SD) of the independent measurements for each target.

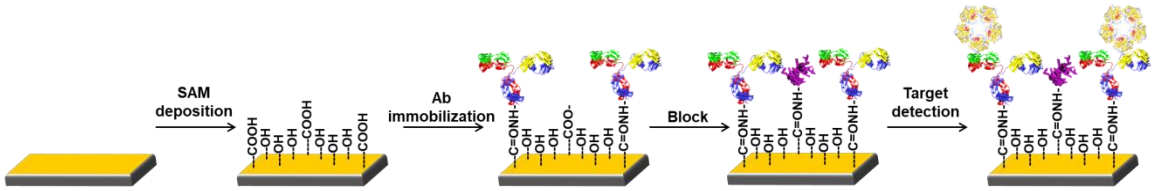

Figure 4 - Schematic representation of the electrochemical impedance approach for antigen-antibody interaction.
Source: Author

3.6. Enzyme Linked Immunosorbent Assay (ELISA)

An indirect ELISA was performed to verify the pairs Ab-target activity, following the protocol from Thermo Scientific (THERMO SCIENTIFIC, 2010). Different protein concentrations (50 µL) were immobilized in the 96-well microplate (from Greiner bio-one) in carbonate/bicarbonate buffer pH 9 overnight at 4 °C. The plate was, then, washed three times with PBS-T, 5 minutes each in agitation, using the Fisher Scientific accuWash. The unbound regions were blocked with 0.1% BSA solution in (blocking buffer; 100 µL) for 1h at room temperature. The plate was washed as before and the wells were incubated with the primary antibody solution (specific for the target immobilized). The Ab solution (concentration 1:500) was prepared in PB pH 7.4 with 0.1% BSA and incubated for 2h at room temperature (50 µL each well). The plate was washed as before and incubated with secondary antibody solution (specific for the specie in which the primary antibody was produced; it is label with HRP enzyme), in PB pH 7.4 and 0.1% BSA. The solution (concentration of 1:5.000) was incubated for 2h at room temperature (50 µL each well). It was washed and incubated with the revelation solution (OPD and substrate G; 100 µL) for 30 min. Then the reaction was stopped with 0.5 M H_2SO_4 and the absorbance was measurement at 492 nm, using the Fisher

Scientific accuSkanGo and the software SkanIt RE 4.1. The negative control was fetuin immobilized against the antibodies of the target analysed and the positive control was with CRP and antiCRP.

3.7. Quartz Crystal Microbalance (QCM) assays.

The quartz crystals were cleaned by immersion in hot piranha solution for 1 min (7 mL H_2SO_4 + 3 mL H_2O_2; *Caution: piranha solution reacts extremely aggressive with organic materials. Please treat with extreme care!*), then were rinsed in distilled water, ethanol and dried with nitrogen. The freshly cleaned crystals were immersed in the ethanolic 1 mM MUA + 6-COH [1:20] solution for 16h at room temperature for SAM deposition. After that, they were cleaned with ethanol, distilled water, dried with nitrogen and mounted in the microbalance cells from qsense. The measurements were done with a peristaltic bomb, using a flow of 180 µL min^{-1}; and QSoft401 software. After crystal frequency calculation, a PB flow was passed through the cells until signal stabilization. Then, the aqueous EDC/NHS solution (600 µL) for carboxylic group activation was injected and incubated inside the cells for 30min (flow off). The cells were cleaned reactivating the Millipore water flow. Then, the PB flow was passed through the cells until signal stabilization. Thereafter, the antibody solution (600 µL) was injected, incubated for 1h (flow off) and cleaned with the PB flow, until signal stabilization. Finally, the unbound carboxylic groups were blocked with a 0.1% BSA solution (600 µL) for 30 min (flow off). Then, the PB flow was reactivated for signal stabilization.

4. Results and discussions

4.1. Self-assembled monolayer optimization.

The first step in the gold electrode functionalization process is the self-assembled monolayer (SAM) deposition. The SAM was composed by 11-mercaptoundecanoic acid (MUA), which is the linker element of the SAM and the 6-mercapto-1-hexanol (6-COH), which is the separator element. This last molecule prevents from a high MUA packaged and the formation of a high insulating SAM. Different MUA – 6-COH proportions were tested, in order to achieve the most stable and reproducible combination. Table 1 shows the mean R_{ct} value of each SAM and the relative standard deviation (RSD), representing the experiment reproducibility. Figure 5 shows the Nyquist plot of each film. The SAMs MUA and MUA + 6-COH 1:1 (Figure 5A and B) showed the highest resistive SAMs. It was not possible to fit the R_{ct} value in any of them with the circuit model used, so the 6-COH concentration was increased. The 1:5 SAM showed higher R_{ct} value (almost 10 times higher) and lower reproducibility (larger intra-electrode RSD value) than 1:15, 1:20 and 1:30 SAMs. As it is shown in Table 1, these three SAMs showed similar R_{ct} and RSD values. SAM 1:20 presented a slightly lower RSD value than the others, so it was chosen for further analysis.

Table 1 - R_{ct} values, stability and reproducibility of the different SAMs tested.

Monolayer	R_{ct} ($k\Omega\ cm^{-2}$)	RSD intra-electrode*
MUA	> 5000	-
MUA + 6-COH 1:1	> 5000	-
MUA + 6-COH 1:5	3761 ± 3072	11.72
MUA + 6-COH 1:15	426 ± 90	1.33
MUA + 6-COH 1:20	394 ± 58	1.10
MUA + 6-COH 1:30	360 ± 95	1.26

*RSD value for one electrode. It was similar in other electrodes.

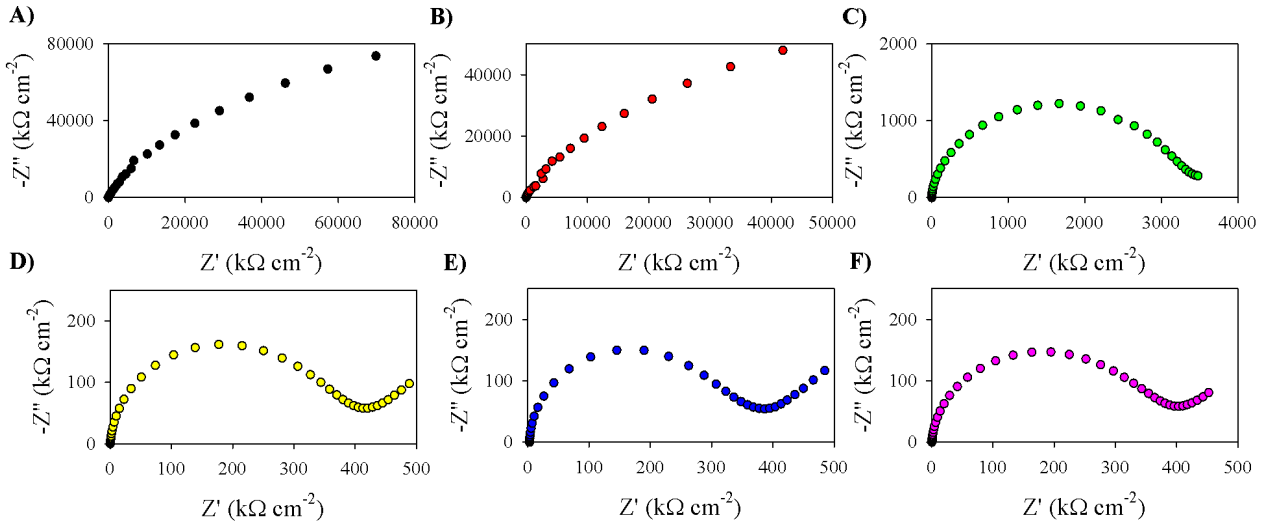

Figure 5 - Nyquist plots of the monolayers tested on gold electrode by different spacer-linker proportion at the formal potential and frequency range 0.1 Hz – 1 MHz. (A) MUA. Active gold electrode area: 0.043 cm^2; (B) MUA + 6-COH [1:1]. Active gold electrode area: 0.05 cm^2; (C) [1:5]. Active gold electrode area: 0.042 cm^2; (D) [1:15]. Active gold electrode area: 0.043 cm^2; (E) [1:20]. Active gold electrode area: 0.047 cm^2; (F) [1:30]. Active gold electrode area: 0.04 cm^2.

Source: Author

After the determination of the monolayer, it was studied the effect of the supporting electrolyte in the EIS measurements. Two supporting electrolytes were tested: 1 M KNO_3, without pH control; and 0.5 M KNO_3 in 12 mM PB, pH 7.4 similar value as the solution of incubations. Consecutive incubations in solutions with different pH could modify the surface charge and cause unspecific EIS variation. The mean R_{ct} value of the impedance measurements performed in 1 M KNO_3 as supporting electrolyte (11 electrodes) was 343 ± 290 kΩ cm^{-2}, the variation intra-electrode was 1.1% and the variation inter-electrodes was 84.7%, showing low repeatability. The measurements performed under pH control (0.5 M KNO_3 in 12 mM PB pH 7.4 as supporting electrolyte) presented a mean R_{ct} value of 638 ± 126 kΩ cm^{-2}, a variation intra-electrode between 0.5-1% and a variation inter-electrodes of 19.8%.This last configuration improved the repeatability of the system, so was assumed as the best condition.

4.2. Faradaic electrochemical impedance spectroscopy assay.

Under the best conditions the gold electrodes were functionalized, following the experimental protocol reported in section 3.4. As an example of the result obtained during the electrode functionalization protocol (it was similar for all the experiments done), here is presented the results of just one electrode, using the protein IL-6 as a model. Figure 6 shows the

voltammograms, Nyquist plots and Bode plots of the bare gold and the functionalization steps. Previous to electrode modification, the gold surface was evaluated by the bare gold voltammogram and Nyquist plot. In the bare gold CV plot of a uniform surface the difference between the oxidation and reduction potential (ΔE_p) should be 58 mV, for single electron transfer reactions (it is considered an acceptable value until 70 mV); the current density ratio between the anodic and cathodic peak has to be closer to the unit according to a reversible system (BARD; FAULKNER, LARRY, 2000); and the bare gold electrode impedance measurement should show a R_{ct} value lower than 200 Ω and the diffusional region has to be predominant (FISCHER et al., 2009). The electrode used showed 66 mV of ΔE_p, the current density ratio between the anodic and cathodic peak was about the unit and showed an R_{ct} value closer to 150 Ω. After the 16h SAM incubation, ΔE_p (350 mV; Figure 6A) and R_{ct} (750 ± 5 kΩ cm^{-2}; Figure 6B) values changed, showing SAM formation. The next functionalization steps (antibody and block) were almost imperceptible by CV. However, there was variation in the EIS measurements.

As a proof of concept, the thiolated electrode was incubated with a monoclonal pure antibody for interleukin-6 (IL-6) protein. As it is shown in Figure 6B, the antibody R_{ct} value (527 ± 9 kΩ cm^{-2}) decreased 30% in comparison with the SAMs value (750 ± 5 kΩ cm^{-2}). This result contradict the fact that impedance should increase after immobilization steps, but two variables affect the electron transfer: the mass and the charge of the elements immobilized at the gold surface. For antibody immobilization, carbodiimide EDC/NHS reaction is used. EDC reacts with carboxylic acid groups (in this case from MUA) to form an active intermediate that will be displaced by nucleophilic attack from primary amino groups which will form an amine bond with the carboxylic acid group. NHS makes the EDC reaction more efficient and forms an NHS ester as intermediate, more stable than the produced only with EDC, so the carboxylic acid groups keeps longer activated (HERMANSON, 2008). The formation of the NHS ester neutralizes the SAM charge, so the impedance signal decreases. An EIS measurement was done after EDC/NHS activation. The EDC/NHS R_{ct} value was 226 ± 10 kΩ cm^{-2}, decreasing 60% the SAM R_{ct} value and after that, the Ab immobilization increased it. The BSA block (578 ± 8 kΩ cm^{-2}) stage increased 10% the Ab (antibody) impedance signal. A stability control was performed at this point (Figure 7). At first, the system showed high variation after the PB incubation (17% of variation; 679 ± 5 kΩ cm^{-2}), but after a new PB incubation, it stabilized, showing a variation of 0.5% between measurements (683 ± 5 kΩ cm^{-2}).

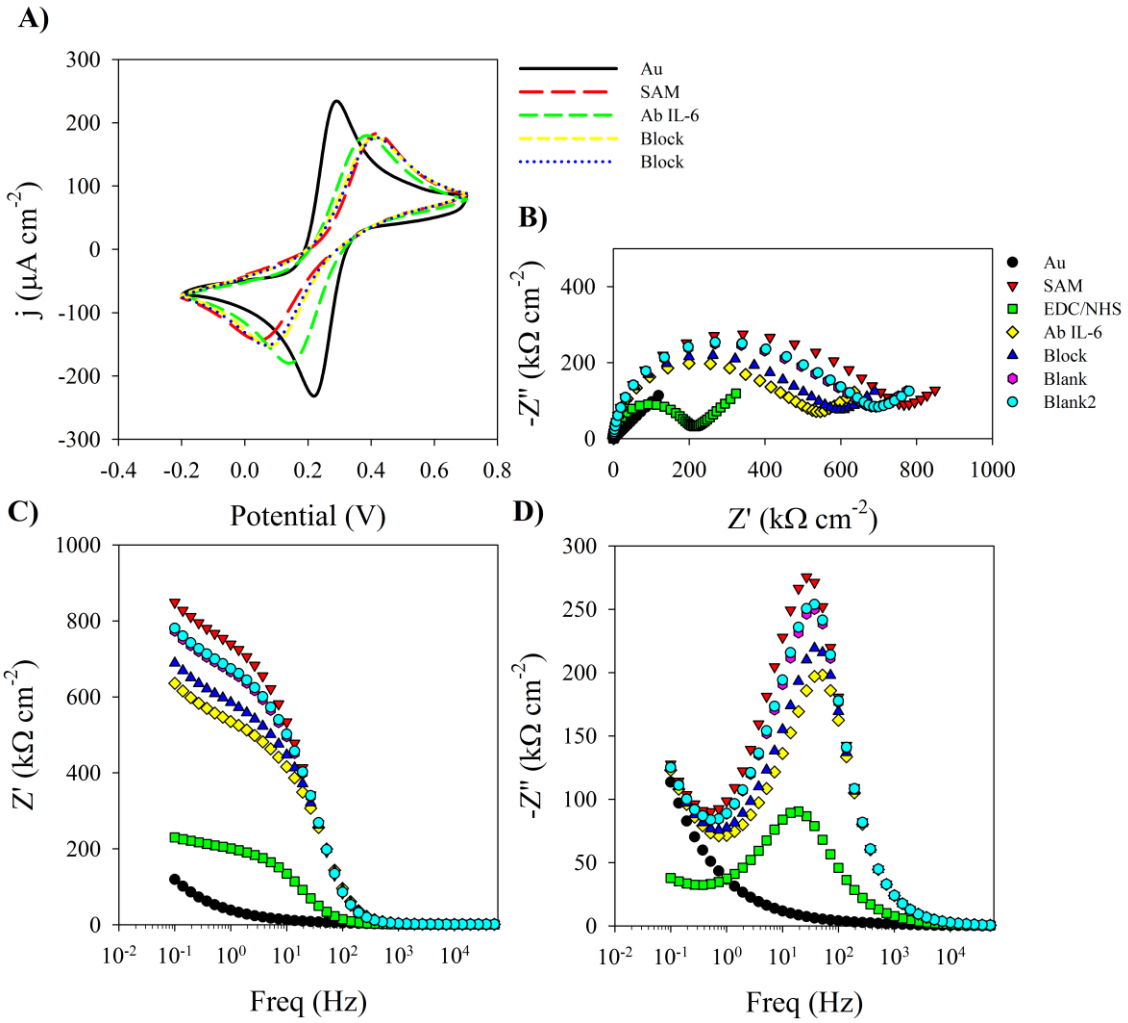

Figure 6 – Cyclic voltammetry, Nyquist and Bode plots of the electrode functionalization process. A) Cyclic voltamogramm; B) Nyquist impedance plot (-Z'' *vs* Z'); C) Bode plot for real impedance (Z' *vs* frequency); D) Bode plot for imaginary impedance (-Z'' *vs* frequency) of SAM, EDC/NHS, antiIL-6, block and blanks measurements, in the disk gold electrode (from Metrohm), in 1 mM $[Fe(CN)_6]^{3-/4-}$, using 0.5 M KNO_3 and 12 mM PB pH 7.4 as supporting electrolyte. Active gold electrode area: 0.047 cm^2.

Source: Author

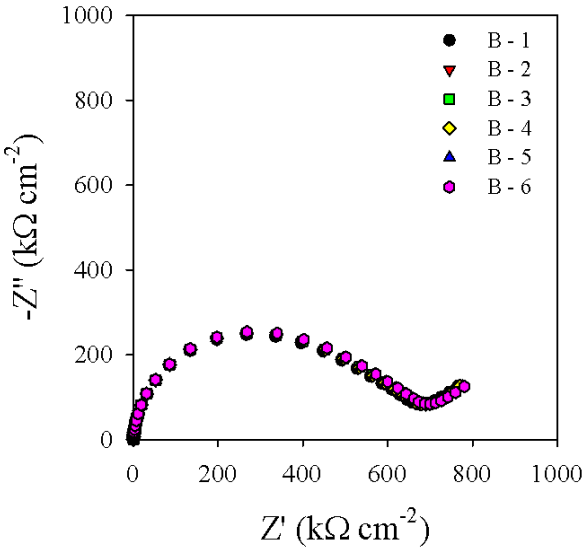

Figure 7 - Nyquist impedance plot (-Z'' *vs* Z') of 6 blanks measurements (B 1-6): B(1-3) EIS measurement after the first PB pH 7.4 incubation; B(4-6) EIS measurements after 30 min PB pH 7.4 incubation), in the disk gold electrode (from Metrohm), in 1 mM $[Fe(CN)_6]^{3-/4-}$, using 0.5 M KNO_3 and 12 mM PB pH 7.4 as supporting electrolyte. Active gold electrode area: 0.047 cm^2.

Source: Author.

As it was reported previously, EIS technique can present unspecific response, so before the target incubation, a negative control was performed (Figure 8). Although it was expected a similar response as the blanks, the R_{ct} (715 ± 3 kΩ cm^{-2}) variation was 5%, slightly higher than the blanks (it was verified by another blank measurement after the negative control; 728 ± 4 kΩ cm^{-2}; 2% of variation). Two IL-6 (target) solutions were tested. The stock solution (1 mg mL^{-1}) was diluted 100 and 1000 times, 10 and 1 µg mL^{-1}, respectively. Those solutions, according to Kiecolt-Glaser et al., are 10^6 times higher than the concentration found in the blood of normal individuals (2003). The lowest IL-6 concentration (1 µg mL^{-1}) increased the R_{ct} value (760 ± 4 kΩ cm^{-2}) 4%, similar variation as the negative control, while the higher concentration had a lower variation, just 1% (R_{ct} value of 768 ± 4 kΩ cm^{-2}), so an specific target response was not achieved.

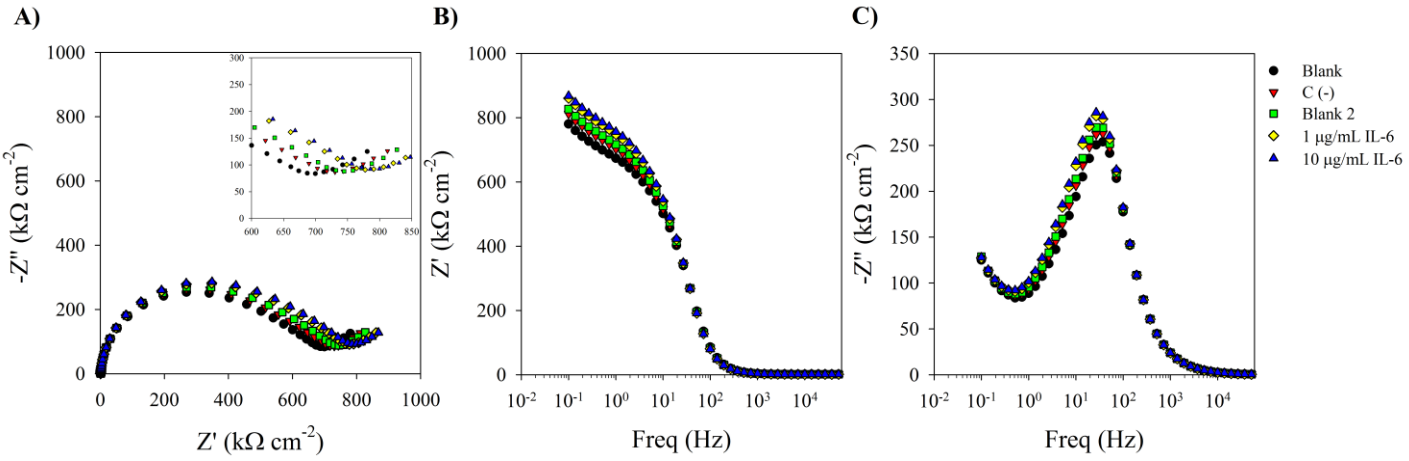

Figure 8 - Nyquist and Bode plots of the target recognition steps. A) Nyquist impedance plot (-Z'' *vs* Z'); B) Bode plot for real impedance (Z' *vs* frequency); C) Bode plot for imaginary impedance (-Z'' *vs* frequency) of blanks, negative control with fetuin and IL-6 solutions, in the disk electrode (from Metrohm), in 1 mM $[Fe(CN)_6]^{3-/4-}$, using 0.5 M KNO_3 and 12 mM PB pH 7.4 as supporting electrolyte. Active gold electrode area: 0.047 cm^2.

Source: Author

Every step involved in the analytical response was study in order to detect the cause of the absence of response, from the activity of the pair antigen-antibody, the Ab immobilization and orientation, to the effect of the thickness of the alkythiol-based SAM.

4.3. Study of the pair antigen-antibody activity.

The activity of the pairs antigen – antibody was studied by ELISA (Enzyme linked inmunosorbent assay). It was performed with four proteins: IL-6, CRP, HER2 and CEA. Table 2 shows the result of the assay. All the proteins showed high activity even in low concentrations. It was tested in the ELISA the two concentrations of IL-6 used in the EIS experiments, 1 and 10 µg mL^{-1}. Unlike the EIS experiments, both concentrations showed high activity in the ELISA test, so, according to those results, the absence of detection observed in the impedimetric biosensor was not caused by inactive AbIL-6-antigen interaction.

Table 2 - ELISA assay results. Absorbance values of the proteins tested.

HER2		CEA		IL-6		CRP	
Conc. (µg mL^{-1})	**Abs** (u.a)	**Conc.** (µg mL^{-1})	**Abs** (u.a)	**Conc.** (µg mL^{-1})	**Abs** (u.a)	**Conc.** (µg mL^{-1})	**Abs** (u.a)
1.00	> 6.000	1.00	2.632	10.00	> 6.000	25.00	> 6.000
0.50	2.960	0.50	0.767	5.00	> 6.000	10.00	2.263
0.10	0.755	0.10	0.023	1.00	2.585	5.00	2.209
0.05	0.320	0.05	0.198	0.10	0.159	1.00	2.164
0.01	0.016	0.01	0.046	0.01	0.317	0.10	2.147
C (-)	0.000	C (-)	0.000	C (-)	0.000	C (-)	0.000

Since the proteins HER2, CEA and CRP showed interaction with their specific antibodies in the ELISA, they were studied separately by EIS. The results (Figure 9 and Table 3) were similar as those achieved in the experiment with IL-6 (section 4.2.). In all the experiments, it was observed the same behaviour: the impedance variation caused by specific target was lower than the blanks variation. As was demonstrated by the ELISA, the absence of response was not due to problems in the interaction activity between the antibody – antigen pairs, so it should be related to the system construction protocol. Thus, the immobilization step was tested by QCM.

Table 3 - Variation values in % of the blanks and the proteins measurements in different proteins.

Protein	**Blanks variation (%)**	**Proteins variation (%)**
HER2	5.2	-4.0 - 6.0
CEA	4.1	1.0 - 3.0
CRP	3.5	2.0 - 4.0

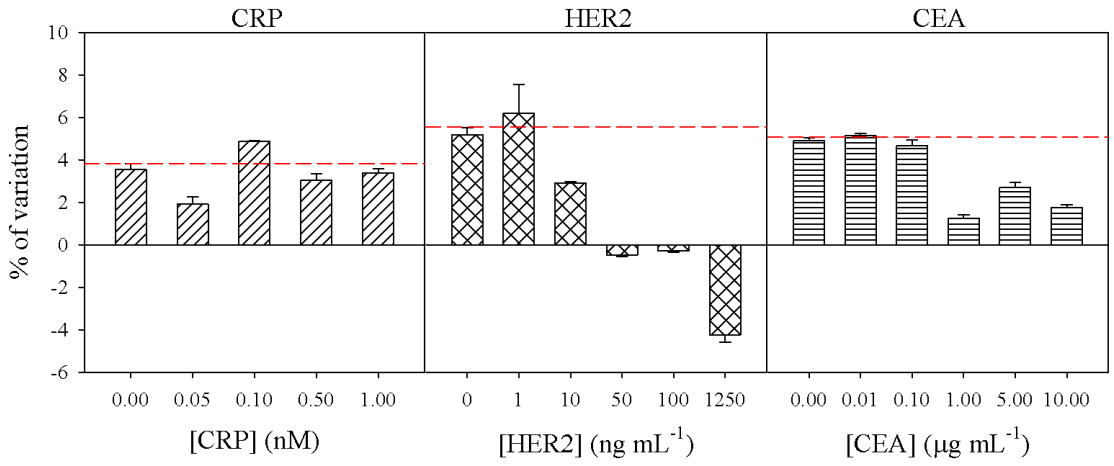

Figure 9 - Relative variation caused by the blanks incubation and the protein solution for 3 different targets: CRP, HER2 and CEA.

Source: Author

4.4. Study of the antibody immobilization step.

It was demonstrated by the ELISA (section 4.3.) that the detection problem was not related to the protein-antigen interaction. The four systems tested (for IL-6, CRP, HER2 and CEA) had in common the antibody immobilization and block step, so they were studied by Quartz Crystal Microbalance (QCM), in order to monitor and quantified each. Modifications of the crystal surface change the frequency proportionally with the number of molecules immobilized. It is possible to quantify the surface mass variation (Δm) by the frequency variation (Δf), using the Sauerbrey relation (Eq. 4) (SAUERBREY, 1959). Proteins in solution present a hydration layer which represent about 0.25 – 0.75 g per gram protein (between 20 – 40% of the mass value) (SAENGER, 1987). According to this, it was assumed that the contribution of the hydration layer was 30% of the mass calculated by the frequency variation (Eq. 5).

$$\Delta m = -c \cdot \Delta f \quad (4)$$

$$\Delta m = -c \cdot \Delta f \cdot (1 - 0.3) \quad (5)$$

where Δm is the mass variation; c is the theoretical QCM sensitivity coefficient (17.7 ng Hz^{-1} cm^{-2} for crystal of 5 MHz); Δf is the frequency variation. Eq. (5) was transformed to Eq. (6) to calculate the number of molecules per cm^2.

$$nº\ molecules/_{cm^2} = \frac{-c \cdot \Delta f \cdot (1-0.3) \cdot N_A}{M_m} \quad (6)$$

where N_A is the Avogadro constant ($6.023 \cdot 10^{23}$ molecules mol^{-1}); M_m is the molecular mass.

As a proof of concept, the QCM test was performed using CRP. Firtsly, it was analysed the EDC/NHS reaction. Problems in the activation reaction could make impossible the attachment of the antibody to the surface, and thus the antibody-antigen interaction. After 30 min EDC/NHS incubation, the frequency varied 5 Hz (upper graph in Figure 10), representing that the SAM-crystal surface experimented a modification with the EDC/NHS reaction. (Note: EDC/NHS graph, Figure 10, showed ups and downs during the incubation due to the formation of bubbles inside the QCM cell).

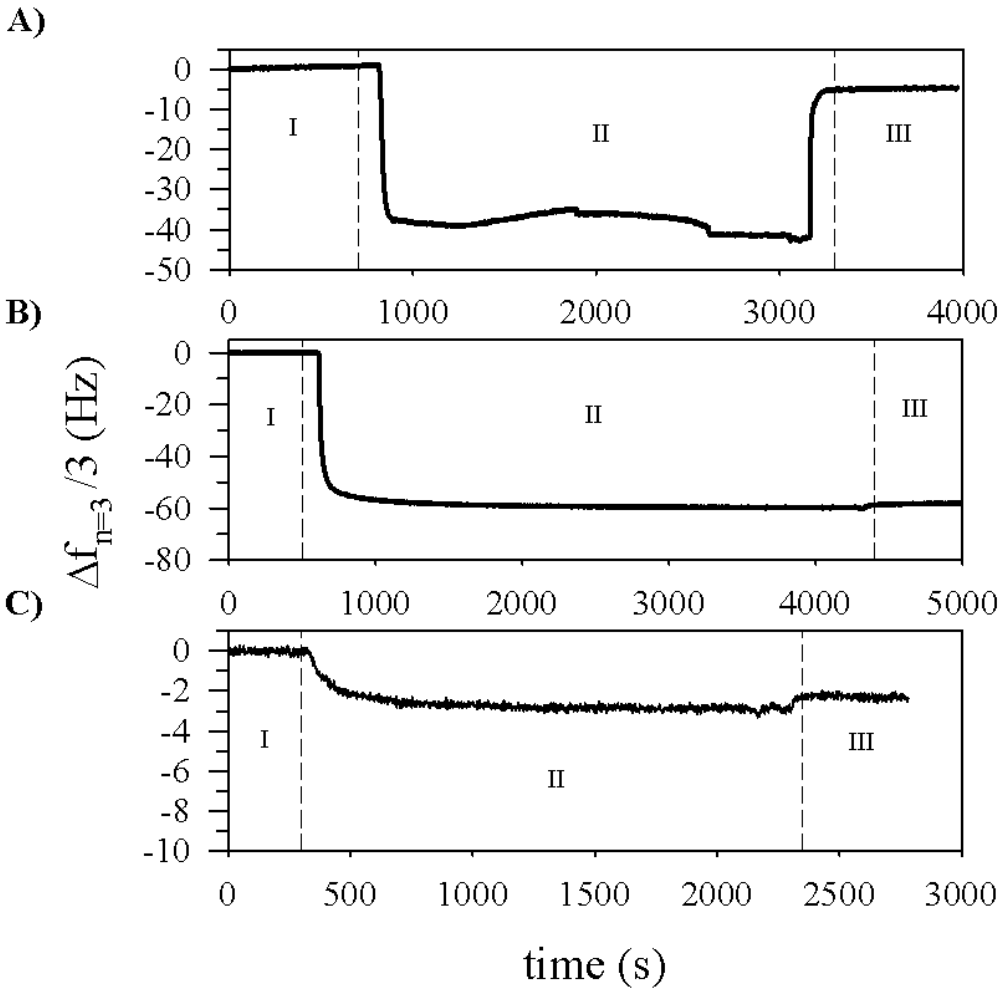

Figure 10 - Characterization of the system construction by QCM. Graphs from top to bottom: EDC/NHS activation; antibody immobilization; and BSA blocking in the quartz crystal. For each procedure, I) signal stabilization with the solution solvent PB (in B and C) or Millipore water (in A); II) incubation with the reagent; III) signal stabilization with the solution solvent.

Source: Author

The incubation with the antibody caused a frequency variation of 60 Hz in both crystals. Applying the Eq. (6), $3 \cdot 10^{12}$ antibody molecules cm^{-2} were attached (similar value in both crystals). The incubation with BSA only decreased 2 Hz the frequency (in both crystals), representing $2 \cdot 10^{11}$ molecules cm^{-2} immobilized. The results showed that it was immobilized 15 times more molecules of antibody than BSA's, so the reason of the lack of response in the EIS experiments was not problems in the antibody immobilization step, nor in the block step.

Therefore, ELISA results (section 4.3.) suggested the antibody-target interaction was not the cause of problem in EIS response and the QCM results demonstrated that the antibody was been covalently immobilized on the thiol surface. The next variable to be analysed was the antibody orientation.

4.5. Oriented-Ab-immobilization with protein A.

An important control point in the antibody immobilization is its orientation. For antibody-target interaction, the variable region (F_{ab}) of the Ab has to be exposed to the solution (Figure 11A). However, the immobilization process by EDC/NHS reaction is random, because the ester generated in the carboxylic group of the SAM can react with any amine group of the antibody (Figure 11B). Protein A is a good tool for control this step. It is a 42 kDa antibody receptor present on the surface of *Staphylococcus aureus*. It presents affinity for the antibody constant region (F_c region) of many types of IgGs (LANGONE, 1982). According to that, the immobilization of the protein A before the Ab immobilization can orient the antibody and improve the target recognition (Figure 11C).

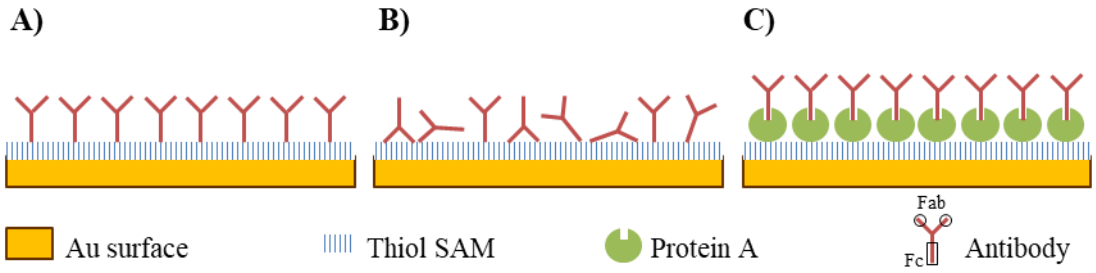

Figure 11 - Scheme of the distribution of the antibody on the thiolated SAM with and without protein A. A) Direct immobilization: ideal Ab organization when it is directly immobilized by the constant region; B) Direct immobilization: real Ab organization when it is directly immobilized; C) Indirect immobilization: expected organization of the Ab previously protein A immobilization.

Source: Author

Protein A (1 mg mL^{-1}) was incubated in PB pH 7.4 for 1h after 30 min activation with EDC/NHS. The free carboxylic groups were deactivated by 5 min immersion in 1 M ethanolamine pH 8.5. Then, the surface was characterized by CV and EIS. Thereafter, it was washed with Millipore water and PB pH 7.4 and incubated for 1 h in the Ab solution. The experiment was performed in two electrodes. In both cases, the variation caused by the incubation of the target solution was similar as the variation caused by the incubations in PB pH 7.4 (blanks) and the negative control, as it is shown in Figure 12 and 13. The blanks and negative control varied between 2 and 4% the R_{ct} value, while the target variation was 0.5-3%, so, once more, detection was not achieve.

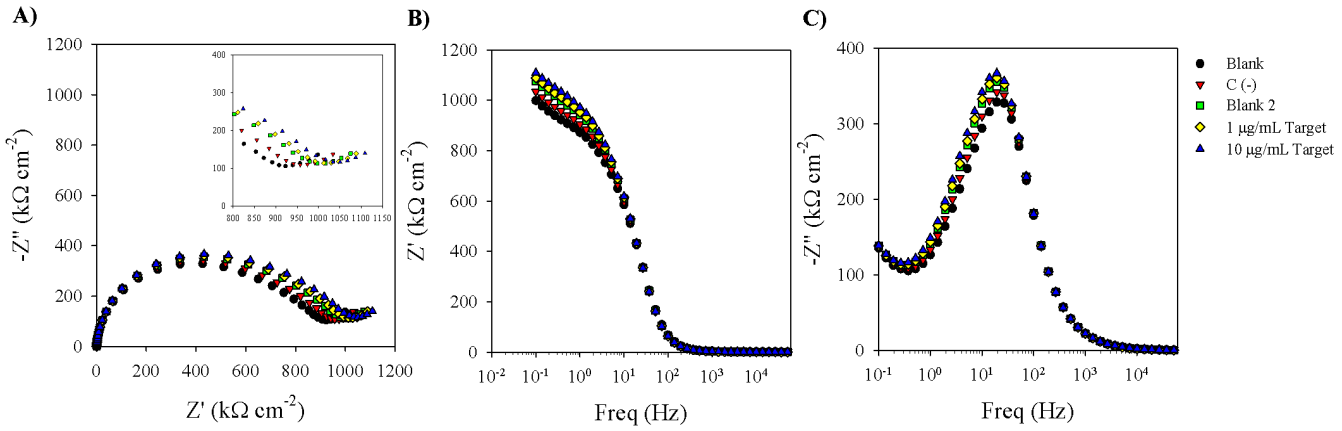

Figure 12 - Nyquist and Bode plots of the target recognition steps using an electrode functionalizated with protein A. A) Nyquist impedance plot (-Z'' *vs* Z'); B) Bode plot for real impedance (Z' *vs* frequency); C) Bode plot for imaginary impedance (-Z'' *vs* frequency) of blanks, negative control with fetuin and target solutions, in 1 mM $[Fe(CN)_6]^{3-/4-}$, using 0.5 M KNO_3 and 12 mM PB pH 7.4 as supporting electrolyte. Active gold electrode area: 0.05 cm^2.

Source: Author

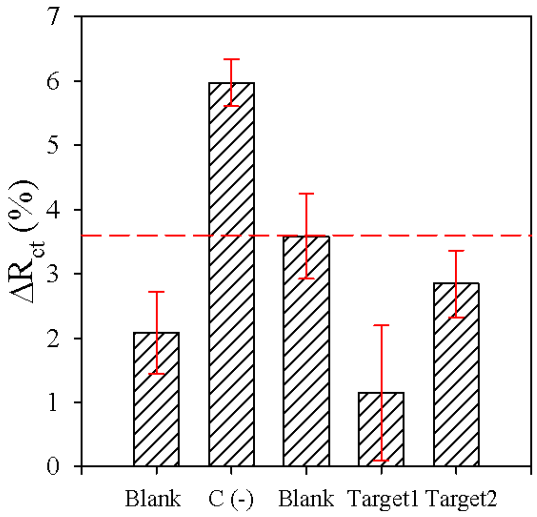

Figure 13 - Relative variation caused by the blanks incubation and the protein solutions, using protein A in the system. Target1 = 1 µg mL^{-1}; Target2 = 10 µg mL^{-1}.

Source: Author

In summary, the ELISA, QCM and EIS with protein A assays showed that the detection failure was not due to problems in the Ab-antigen interaction or in the Ab immobilization or orientation. After that, it was studied if the low system sensitivity was caused by the high thiolated-SAM thickness by an EQCM assay with cysteine monolayer.

4.6. Simultaneous QCM and EIS assay with cysteine monolayer.

The effect of the SAM thickness was studied by a simultaneous QCM and EIS assay with a cysteine monolayer in a quartz crystal, using as a reference the protocol of Simão et al. They used an ultrathin monolayer of cysteine for build a sensitive and reproducible system. They incubated 1 µL of 25 mM cysteine and allowed to dry (SIMÃO et al., 2016). Here, the 25 mM cysteine solution was incubated in flow in the QCM cell for 20 min, so the cysteine deposition was monitored. The others functionalization steps were similar as the reported in section 3.7. All of them were monitored by QCM and, then, characterized by CV and EIS (after each modification, the crystal was mounted in the electrochemical microbalance cell from qsense and characterized in 1 mM $[Fe(CN)_6]^{3-/4-}$ in 0.5 M KNO_3 and 12 mM PB pH 7.4.). Figure 14 shows the QCM graph of each crystal modification step and Table 4 shows the number of molecules attached after each functionalization step, using Eq. (4), (5) and (6), according to the QCM results.

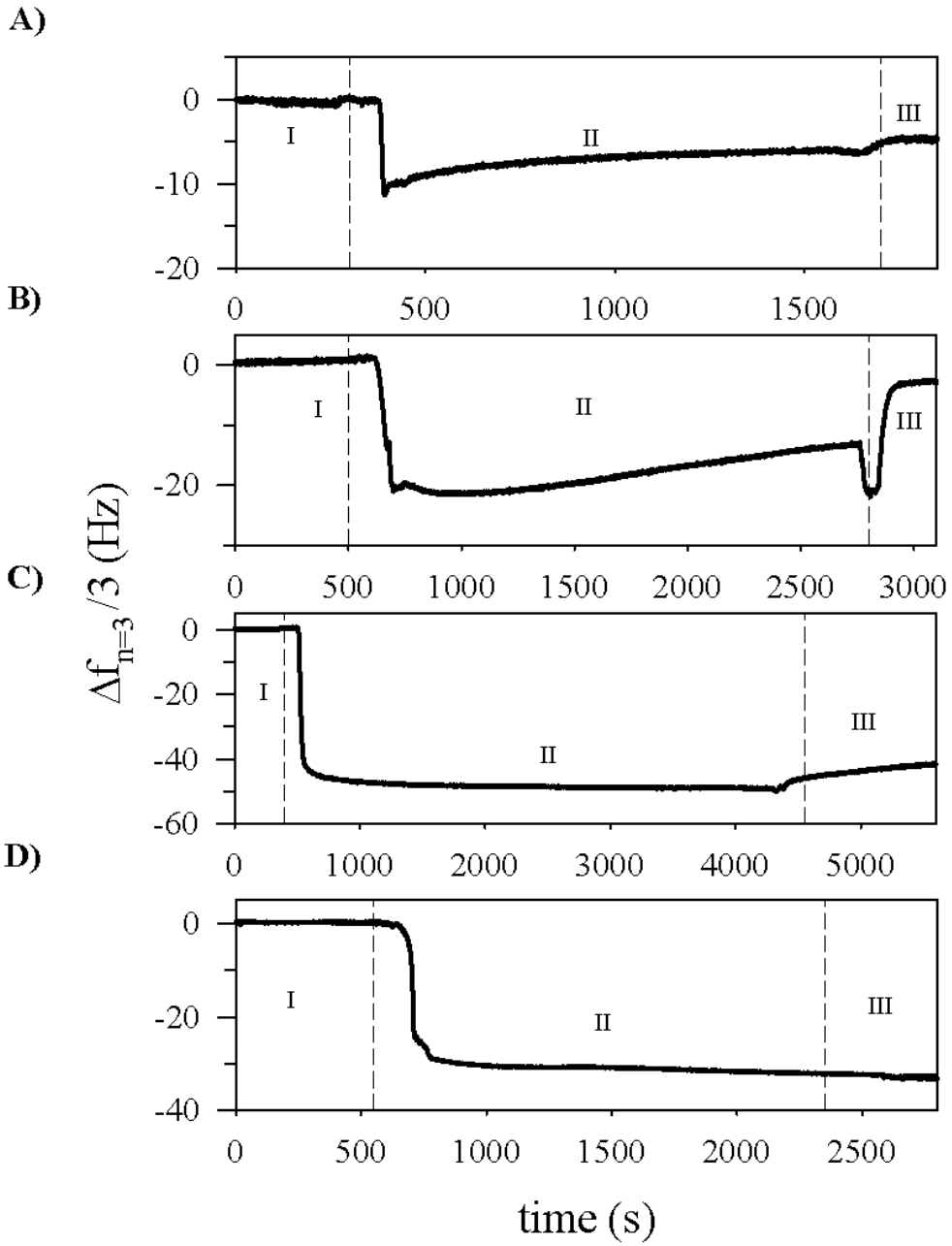

Figure 14 - QCM results of the cysteine based system. Graphs from top to bottom: Cysteine immobilization; EDC/NHS activation; antibody immobilization; and BSA blocking in the quartz crystal. For each procedure, I) signal stabilization with the solution solvent PB (in A, C and D) or Millipore water (in B); II) incubation with the reagent; III) signal stabilization with the solution solvent.

Source: Author

Table 4 - Absolute frequency variation, mass variation and number of molecules per cm^{-2} of the QCM assay for the cysteine, antibody and BSA immobilization.

Molecule	Absolute Δf (Hz)	Δm (ng cm^{-2})	Nº molecules per cm^2
Cysteine	5	88.5	$4 \cdot 10^{14}$
Antibody	42	520.4*	$2 \cdot 10^{12}$
BSA	30	371.7*	$3 \cdot 10^{12}$

*Δm of antibody and BSA represents the absolute mass variation subtracting the mass of the solvation layer (aprox. 30% of the mass), calculated by Eq. (6)

As it is shown in Table 4, QCM results demonstrated the construction of the cysteine-based biosensor. It was showed the immobilization of the cysteine monolayer, the immobilization of the antibody and the BSA blocking of the free carboxylic groups. After that, the platform was tested with the target solutions.

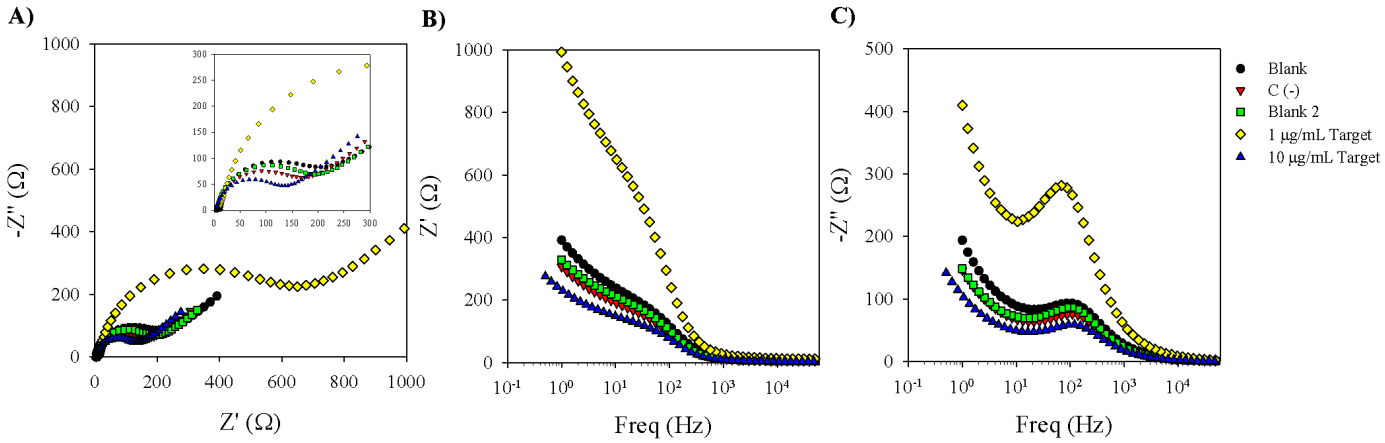

Figure 15 - Nyquist and Bode plots of the target recognition steps using an electrode functionalizated with cysteine monolayer. A) Nyquist impedance plot (-Z'' *vs* Z'); B) Bode plot for real impedance (Z' *vs* frequency); C) Bode plot for imaginary impedance (-Z'' *vs* frequency) of blanks, negative control with fetuin and target solutions, in 1 mM $[Fe(CN)_6]^{3-/4-}$, using 0.5 M KNO_3 and 12 mM PB pH 7.4 as supporting electrolyte. Crystal geometric area: 154 mm^2.

Source: Author

The target response was only characterized by EIS (Figure 15), since the concentrations were not high enough to be detected by QCM (1 and 10 µg mL^{-1}). The EIS measurements showed a high variation (230%) between the blank measurement (187 ± 1 Ω) and the 1 µg mL^{-1} target concentration (610 ± 2 Ω). However, after the incubation with the 10 µg mL^{-1} target, the R_{ct} (124 ± 2 Ω) decreased 80%, compared with the R_{ct} value of the 1 µg mL^{-1} solution. This unexpected behaviour could be due to an ineffective wash step, surface damage during the cell changing or the destruction of the functionalized thiolated crystal surface. This last option was included, considering the information reported by Vogt et al. (2016).

4.7. Study of the MUA + 6-COH 1:20 self-assembled monolayer defects.

The last hypothesis suggested was based on the effect of the organization of the film. It was suggested that the distribution of the 6-COH and MUA molecules in the electrode surface was not ideal (Figure 16A); instead, the 6-COH was forming big areas or *islands*, leaving the MUA molecules too separated, so the charge transfer in the recognition event was not as block as expected (Figure 16B); also, it could present free-SAM areas (pinholes) in the electrode surface which facilitates even more the electron transfer (Figure 16C). Those coverage defects could limit the impedimetric effect of the functionalization steps, thus little surface variations (Ab-target interaction) would not be detected, since the redox probe can freely access the electrode surface. This issue was studied following the protocol of Lee and Lennox (2007). They described a new method for studied coverage defects using ferrocenyldodecanethiol by CV in 1 M $HClO_4$. The thiol-SAM modified gold electrode was briefly immersed (5 seconds) in a solution of 2 mM ferrocenyldodecanethiol. According to Lee and Lennox, this short exposure was sufficient for ferrocenyldodecanethiol molecules label on the free-SAM spaces, so changes in CV would be detected.

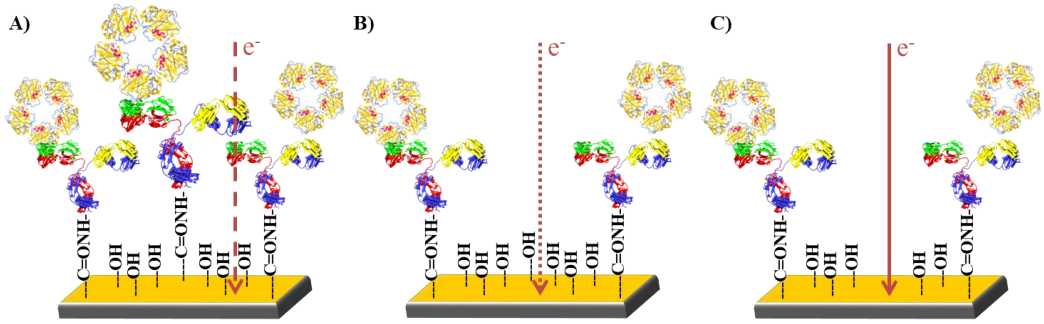

Figure 16 - Thiolated SAM distribution on the gold electrode surface. A) Ideal distribution and behaviour of the functionalized electrode; B) hypothetical distribution of the SAM 1:20; C) hypothetical real distribution and deposition of the SAM 1:20 on the gold electrode surface.
Source: Author

Here, it was used 11-ferrocenylundecacethiol (11-FcC) and $NaClO_4$ for CV measurements (the original protocol was changed because laboratory availability; both reagents were purchased from Sigma). The results are shown in Figure 17. CV in 1 mM $[Fe(CN)_6]^{3-/4-}$ was performed to guarantee the SAM deposition after the 16h incubation. The non-faradaic CV SAM measurement was performed to confirm the absence of redox activity, as it is shown in Figure 17B. After the 5-second-incubation of the 2 mM 11-FcC solution, redox activity

appeared, showing that the SAM presented defects, since the 11-FcC molecules had space on the gold surface to attach.

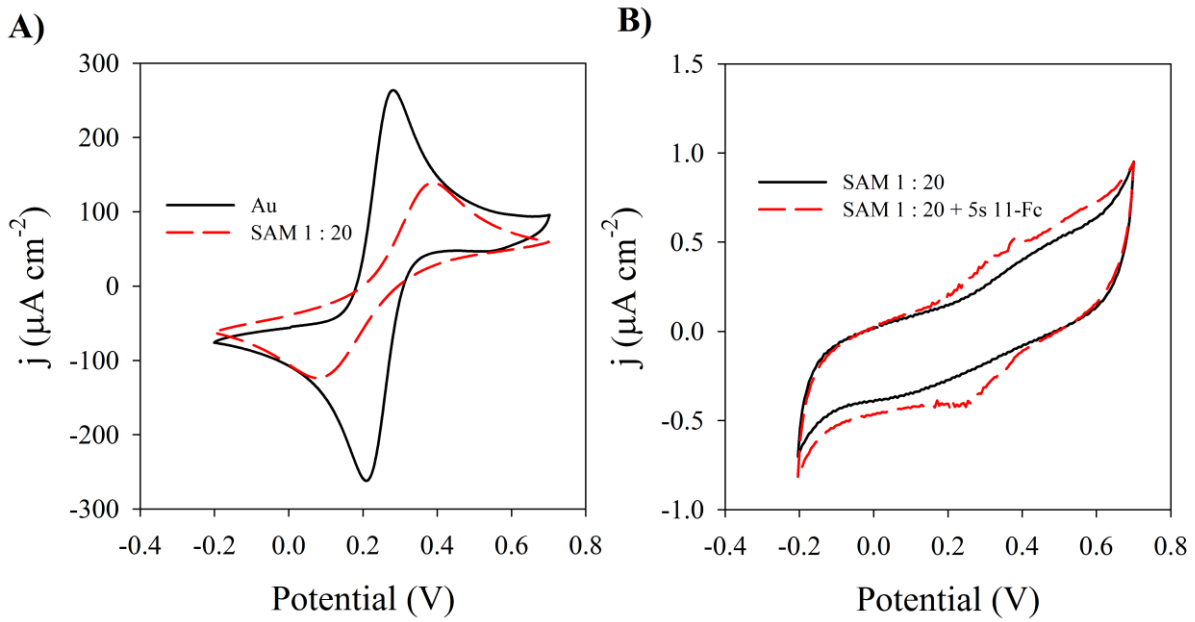

Figure 17 - Faradaic and non-faradaic cyclic voltamogramm of the bare gold and the [1:20] SAM in A) 1 mM $[Fe(CN)_6]^{3-/4-}$, using 0.5 M KNO_3 and 12 mM PB pH 7.4 as supporting electrolyte; B) 1 M $NaClO_4$ before and after 5 seconds incubation in 2 mM 11-FcC. Active gold electrode area: 0.05 cm^2.

Source: Author

In order to control the deposition of the SAM elements and try to reduce the coverage defects, a second experiment was performed. In this case, the mix SAM was deposited separately; firstly, 1 mM 6-COH solution was incubated for 1h; secondly the electrode was incubated in a solution of 1 mM MUA for 2h. After each incubation, the surface was characterized by non-faradaic and faradaic measurements (in 0.5 M KNO_3 and 12 mM PB pH 7.4 and 1 mM $[Fe(CN)_6]^{3-/4-}$ in 0.5 M KNO_3 and 12 mM PB pH 7.4, respectively) to monitor the impedance and capacitance contributions of the elements of the mix SAM. As it is shown in Figure 18 and Figure 19A, it was a variation in the R_{ct} and in the C_r values after the immobilization of the 6-COH and MUA. Also, the current density decreased after the immobilizations, comparing with the gold voltammogram. It was demonstrated that the resulting SAM was a contribution of both thiol molecules.

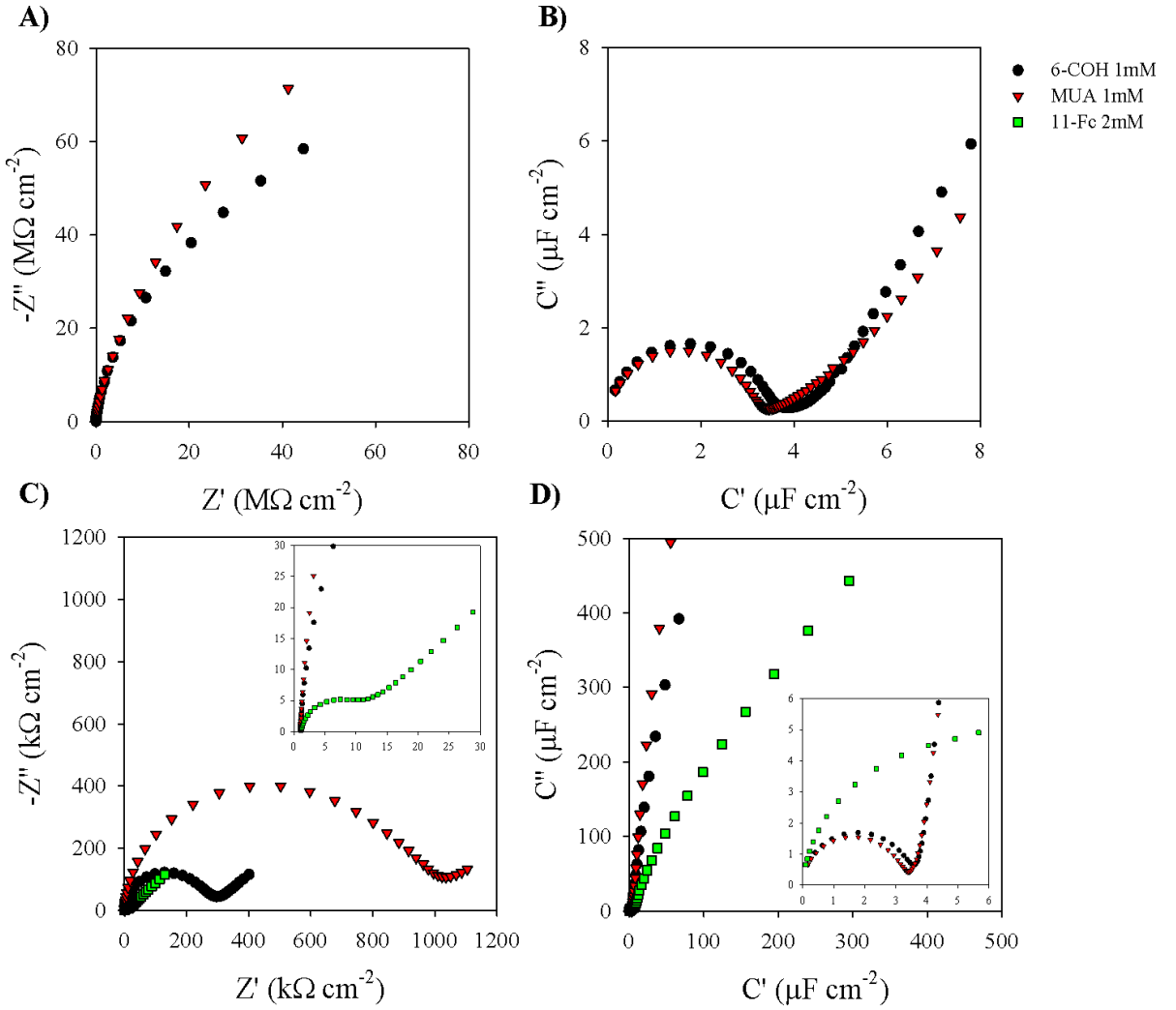

Figure 18 -Nyquist plots of the sequential SAM formation. A) Non-faradaic impedance Nyquist plot; B) Non-faradaic capacitance Nyquist plot of 1 mM 6-COH and 1 mM MUA deposition in 0.5 M KNO_3 and 12 mM PB pH 7.4; C) Faradaic impedance Nyquist plot; D) Faradaic capacitance Nyquist plot of 1 mM 6-COH, 1 mM MUA and 2 mM 11-FcC deposition in 1 mM $[Fe(CN)_6]^{3-/4-}$, using 0.5 M KNO_3 and 12 mM PB pH 7.4. Active gold electrode area: 0.047 cm^2.

Source: Author

Again, the SAM defects were analysed by Lee and Lennox protocol (2007). In this case the change in the voltammetry in $NaClO_4$ after the 11-FcC incubation was not as perceptible as in the previous experiment, because of the background noise. However, it was detectable by CV and EIS faradaic measurements. As is shown in Figure 18C and D and Figure 19A, after the 11-FcC incubation, the electron current increased and, so, the impedance decreased, maybe, because the 11-FcC immobilized could contribute in the electron transfer, acting as a signal amplifier. Although, the formation protocol of the mix SAM was changed, the presence of pinholes seemed to persist.

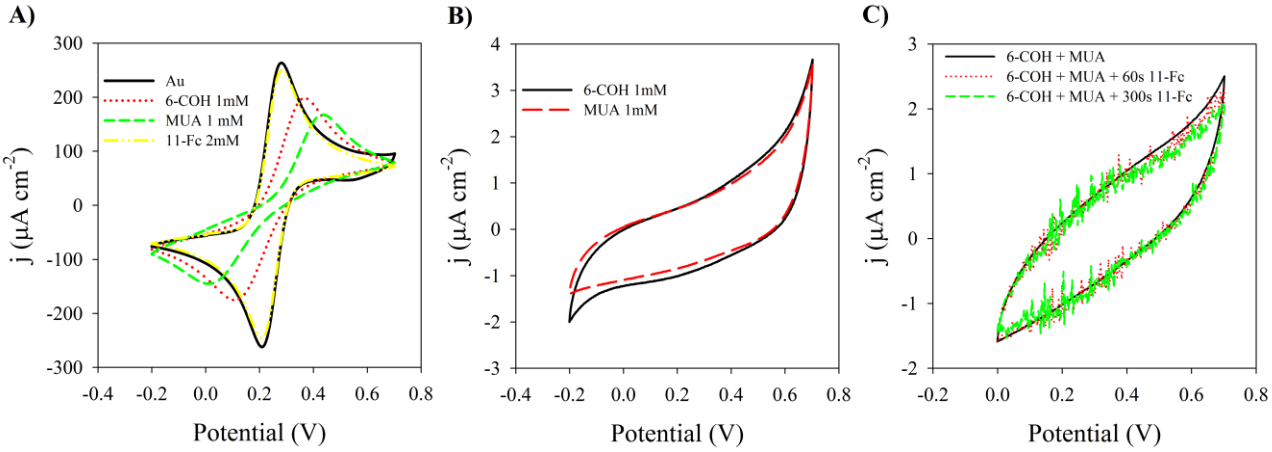

Figure 19 - Faradaic and non-faradaic cyclic voltamogramm of the bare gold and 6-COH, MUA and 11-FcC deposition, in A) 1 mM $[Fe(CN)_6]^{3-/4-}$, using 0.5 M KNO_3 and 12 mM PB pH 7.4 as supporting electrolyte; B) 0.5 M KNO_3 and 12 mM PB pH 7.4; C) 1 M $NaClO_4$ after and before 60s and 300s incubation with 2 mM 11-FcC solution. Active gold electrode area: 0.047 cm^2.

Source: Author

Another parameter was analysed to confirm the presence of defects in the previous SAM, following the procedure of Boubour and Lennox (2000). They studied the ionic insulating properties of thiol-based self-assembled monolayers by a non-faradaic EIS measurement and measured the phase angle (φ) at the low-to-medium frequency (1 - 10^3 Hz). The system was modelled using the equivalent circuit from Lehr, et al. (2017), being the capacitance of the double layer (C_{dl}) in series with the resistance of the solution (R_s). The phase angle was measured at 10^3 Hz, since at lower frequencies the field induced motions can lead to ionic movement and variations in the phase angle would not be indicative of just film defects (LEHR et al., 2017). A perfect structured SAM would behave as an ideal capacitor, in which the gold surface would be one of the plates and the ions physisorbed at the SAM/solution interface as the second plate. In this case, the phase angle (φ) at 10^3 Hz would be $\geq 87°$. This value would decrease ($\varphi < 87°$) with the presence of pinholes on the surface, since the thiolated-SAM and the electrode surface would not form an ideal capacitor. They included a resistive component, related to the ionic migration. Thus, the phase angle could be a good parameter to indicate the presence of defects of the SAM. The phase angle was analysed in the results of the experiment before (sequential SAM), firstly the deposition of 6-COH and then of the deposition of MUA and the formation of the final SAM (Figure 20). The phase angle value was $\varphi = 85°$. The value was $\varphi < 87°$, slightly lower than that showed in perfect films. Although the formation protocol of the film on the electrode surface was changed, it

still showed defects. However, with this new protocol the number of defects seemed to be lower than the overnight incubation.

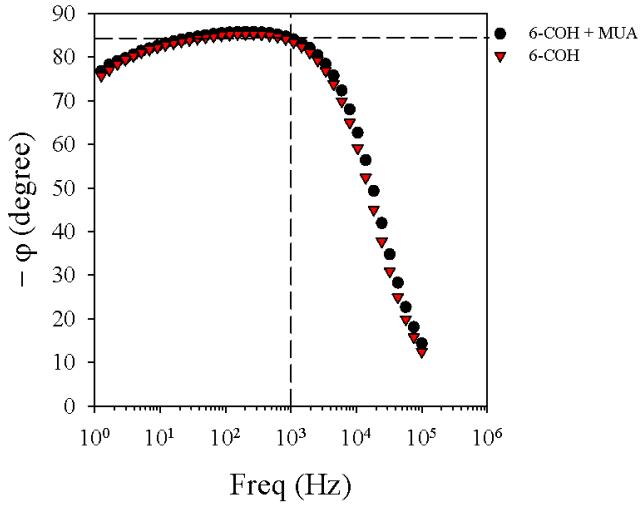

Figure 20 - Study of the the phase angle (***φ***) of the SAM constructed in sequential as an analyses of the presence of pinholes.

Source: Author

Lee and Lennox reported the presence of defects in a self-assembled monolayer composed by a thiol with 14 carbons and incubated for 72h, so even having SAMs incubated for a longer period of time, causing higher thickness and higher level of crystallization, still present defects. As they described, coverage defects in thiolated SAMs are an important issue in biosensors based on electron transfer process with redox probe in solution, because the insulation defects would allow a free electronic and ionic migration from the solution to the electrode surface (BOUBOUR; LENNOX, 2000; LEE; LENNOX, 2007). Hence, the presence of pinholes could be the reason of the lack of specific response in the impedance-based experiments. Electrochemical capacitance spectroscopy (ECS) with faradaic configuration can be the solution of this problem. Although the SAMs can present the same defects, the fact that the redox probe is confined on the electrode surface (redox SAM) can reduce the effect of the coverage defects.

4.8. Faradaic impedance-derived capacitance assay.

Faradaic ECS, as was mentioned before, is based on the electrochemical capacitance ($C_{\overline{\mu}}$) associated with the electrochemical potential of the density-of-states of the redox SAM (LEHR et al., 2017). The capacitance at the formal potential (redox capacitance, C_r), related with the density-of-state of the monolayer, is greatly higher than the capacitance at the redox out (out of the formal potential), associated with the non-faradaic processes, like those correlated with the coverage defects. In contrast with the impedance-based technique, in the faradaic ECS approach the modifications steps of the electrode would have a higher contribution on the redox capacitance than the SAM defects. Because of this, an ECS-based system was used, in order to resolve the EIS-based system experimental problems. It was used a SAM based on a redox peptide, developed and firstly used in ECS experiments by Piccoli, et al**.** (2018), using a DNA aptamer for CRP detection. The peptide consisted in Fc-Glu-Ala-Ala-Cys and was manually produced by laboratory of Prof. Eduardo Maffud (Institute of Chemistry, São Paulo State University, UNESP). The process of surface modification was similar as that used in the EIS experiments, but those modifications were monitored by the redox capacitance (C_r), calculated by the EIS measurements. The results were compared with those obtained by Piccoli, et al. (2018). The experiment was done in triplicate (three electrodes), but here it is shown just the results of one of them, as an example, since all of them showed similar results. Before the construction of the biosensor, it was verified the formation of the redox peptide SAM by CV and EIS at the formal potential and at the redox-out potential (Figure 22A and B) and its stability (Figure 21). The voltammetry plot of the SAM showed a similar conductivity of the SAM from Piccoli, et al. (2018) (near ± 20 µA cm^{-2}) and the current density ratio between the anodic and cathodic peak has to be closer to the unit according to a reversible system. The stability was analysed by nine consecutive EIS measurements (Figure 21) and it was calculated the standard and relative standard deviation. The redox capacitance value of the SAM was 260 ± 3 µF cm^{-2} (representing a 1.2% of variation between the measurements), similar value as that obtained by Piccoli, et al. (2018) (267 ± 7 µF cm^{-2}, 2.7% of variation). The C_r of the SAM at the redox out potential (0.1 V) was 4.70 ± 0.04 µF cm^{-2}, slightly lower than that from Piccoli, et al. (2018), maybe because the electroactive film did not present as much defects. Those results guaranteed the film formation on the gold electrode surface. Figure 22 shows the cyclic voltammetry, the capacitance Nyquist plot and the Bode plots of the development of the biosensor platform.

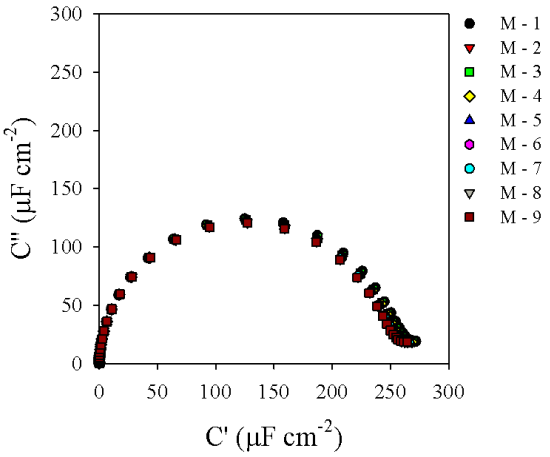

Figure 21 - Redox peptide SAM stability. M1-9: nine consecutive EIS measurements of the electroactive film. Active gold electrode area: 0.045 cm^2.

Source: Author

Upon the immobilization of the Ab to the previously activated SAM, the conductivity of the system decreased (Figure 22A) and the Cr value decreased 40% (156 ± 1 µF cm^{-2}, 0.6% of variation), confirming the antibody immobilization (Figure 22B). The variation was also perceptible in the Bode plots (Figure 22C and D). The variation of the blocking step was just of 4% (150 ± 1 µF cm^{-2}, 0.7% of variation), as can be observed in all plots of Figure 22.

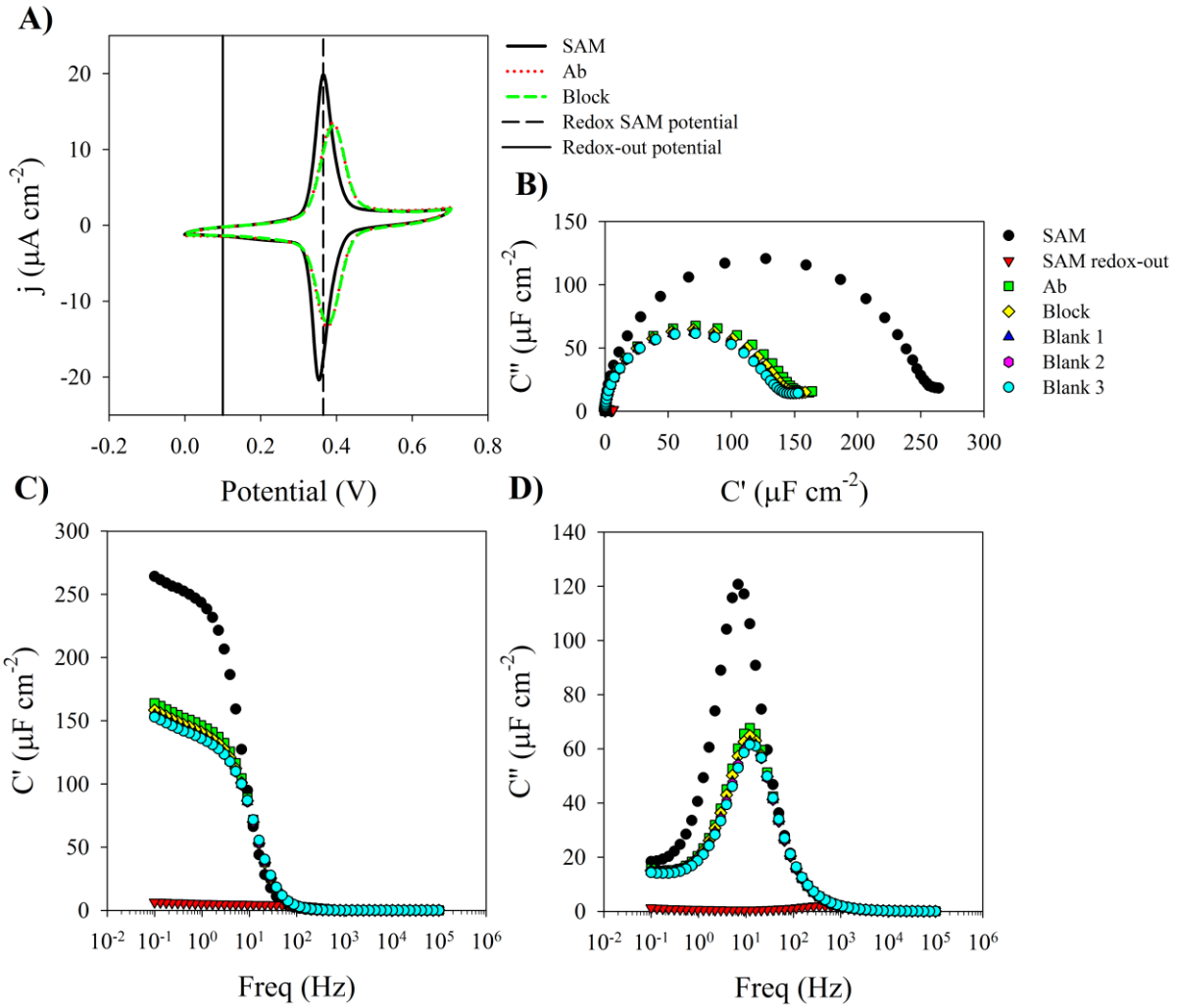

Figure 22 – Cyclic voltammogram, Nyquist and Bode plots of the ECS based electrode functionalization process. A) Cyclic voltammogram; B) Nyquist capacitance plot (-C'' *vs* C'); C) Bode plot for real capacitance (C' *vs* frequency); D) Bode plot for imaginary capacitance (-C'' *vs* frequency) of SAM, SAM at de redox-out potential, antiIL-6, block and blanks measurements in 20 mM TBA as supporting electrolyte. Active gold electrode area: 0.045 cm^2.

Source: Author

The stability of the system was then tested (Figure 23). It was performed three blanks measurements and they showed a 0.7% of variation between them (143 ± 1 µF cm^{-2}), so the system was quite stable before the measurements with the specific target.

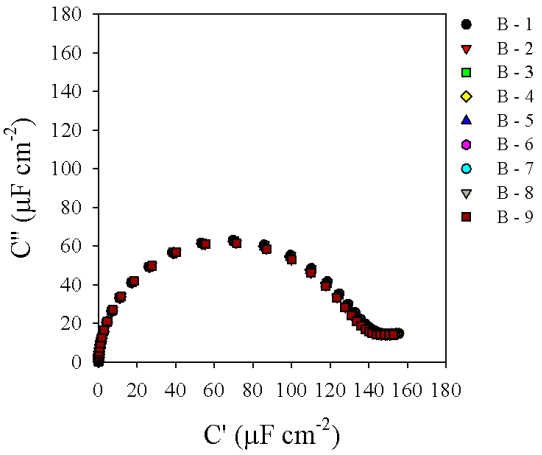

Figure 23 - Study of the stability of the biosensor surface for the protein IL-6. B1-3: triplicate EIS measurements after 30 min immersion in PB. B4-6: triplicate EIS measurements after a second immersion in PB during 30 min. B7-9: triplicate EIS measurements a third immersion in PB for 30 min. Active gold electrode area: 0.045 cm^2.
Source: Author

It was used six concentrations of the protein IL-6: 0.02, 0.05, 0.50, 1.00, 5.00 and 10.00 µg mL^{-1}. The results are shown in Figure 24. As it can be observed, the system was not responsiveness to of the protein solution tested.

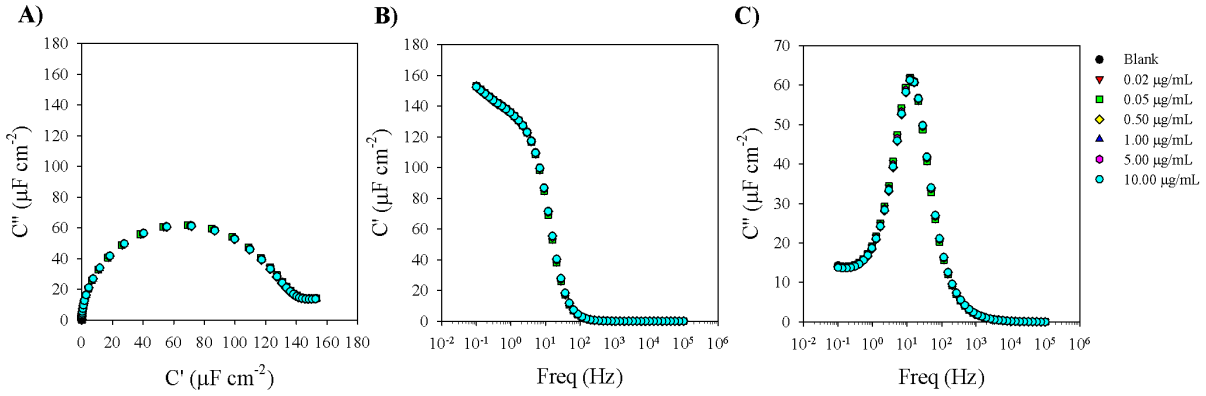

Figure 24 - Nyquist and Bode plots of the detection of the protein IL-6. A) Nyquist capacitance plot (-C'' *vs* C'); B) Bode plot for real capacitance (C' *vs* frequency); C) Bode plot for imaginary capacitance (-C'' *vs* frequency) in 20 mM TBA as supporting electrolyte. Active gold electrode area: 0.045 cm^2.
Source: Author

This lack of response was in disagreement with the results presented by Piccoli, et al. (2018) for the protein CRP (Figure 25). They showed variation for every CRP concentration, from the lowest until de highest one, with a LOD of 7.2 ± 2.4 pM (0.85 ± 0.28 ng mL^{-1}).

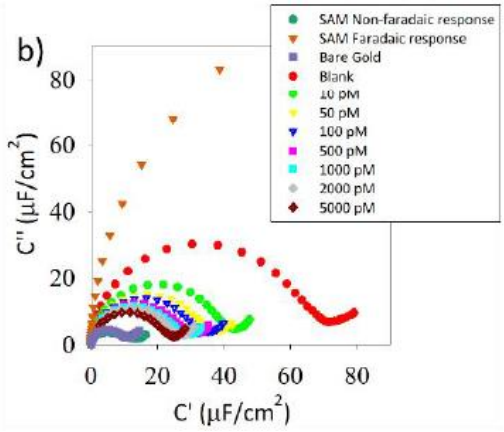

Figure 25 - Nyquist impedance plot of the detection of the protein CRP from Piccoli, et al.
Source: (PICCOLI et al., 2018) *with the permission of the authors*.

Interleukin-6 is lower than the rest of the protein tested in an ECS-based system. In our group, it has been already developed system for different proteins. Similar ECS systems with similar electroactive SAMs have been used for several proteins. Comparing those results, it is possible to correlate the weight of the protein used and the sensitivity of the system (change in the relative response (%) over the change in protein concentration (mol L^{-1})). As an example, the system based on a SAM formed by 16-MHDA (16-mercaptohexanodecanoico) and 11-FcC [1:1] has been successfully used for the detection of the proteins CRP, Ab α-sync and NS1. NS1 is a 46 kDa protein. Cecchetto, et al. (2017) developed an ECS system for the detection of NS1, achieving a linear correlation between the relative response of $1/C_r$ and the protein concentration with a change in the relative response (%) over the change in protein concentration (mol L^{-1}) of 14. Fernandes, et al. (2015) used the similar system for the detection of CRP (118 kDa) and the antibody of the receptor α-sync (Ab α-sync; 150 kDa). They achieved analytical curves with sensitivity of 30 and 84, respectively. Thus, the smallest protein (NS1) showed the lowest sensitivity. That means that the relative response per variation of the protein concentration of the NS1 system is lower than the achieved with the systems with bigger proteins (CRP and Ab α-sync). The systems for CRP and Ab α-sync in Fernandes, et al. (2015) were constructed with biological receptors with different weight. In the first, the biological receptor was an Ab anti-CRP, a molecule of 150 kDa; while in the Ab α-sync system the biological receptor was a molecule of 14.4 kDa (cellular receptor of Ab α-sync). The α-sync system showed an analytical curve with a slope almost 3 times higher than the CRP system. This difference in sensitivity could be attributed not only to the previous correlation (higher protein weight, increase system sensitivity), but also to the difference in weight of the biological receptor and the target. This study of the influence of the biological

receptor weigh in the system sensitivity was also reported by Piccoli, et al (2018). They compared the results obtained with a system using an Ab as a receptor and a system with a DNA aptamer as a receptor, both for CRP detection. In the Ab-based system, the change in the relative response (%) over the change in protein concentration (mol L^{-1}) of the analytical curve was 11.4 ± 1.1, while in the homologue system with the aptamer as a receptor the variation was 87.7 ± 3.7, almost 8 times higher than the Ab's system. So, systems with smaller biological receptor than the target used could show higher sensitivity than systems in which the target is lower or similar as the receptor. The IL-6 system proposed in this work was compounded by an Ab of 150 kDa and the target of 26 kDa (big receptor and small target). IL-6 is 1.8 times lower than NS1, 4.5 times lower than CRP and 5.8 times lower than Ab α-sync, so, according with the previous correlation, the lack of analytical response in the ECS system could be due to the small molecular weight of the protein IL-6, 5.8 times lower than the antibody (bioreceptor). The work of Piccoli, et al. (2018) is the first report of that peptide-based electroactive monolayer, so it is not possible to make that correlation. However, it is assumed a similar behaviour.

4.9. Electrochemical analysis of an electroactive film based system with redox probe in solution.

During the study of the defects present in the thiol-based SAM (section 4.7), it was observed a diminution of the charge transfer resistant (R_{ct}) (Figure 18C) and an increase in the conductivity of the system after 11-FcC immobilization (Figure 19A). The effects of the presence of the redox probe in both, confined on the surface and in solution, was analysed deeper, using a redox peptide-based SAM and varying the $[Fe(CN)_6]^{3-/4-}$ concentration in 20 mM TBA solution. This configuration allowed controlling the total amount of iron ions involved on the process, due to it can be measured the number of redox peptide molecules on the SAM and the amount of redox probe in solution. The changes were monitored by EIS measurements in three different potentials: the formal potential of the redox peptide, 0.38 V; the formal potential of the $[Fe(CN)_6]^{3-/4}$ in 20 mM TBA, 0.22 V; and the half-wave potential of both redox probes, 0.30 V. The measurements were done in 20 mM TBA and in 20 mM TBA with 0.1, 0.2, 0.3, 0.5, 1.0 and 2.0 mM $[Fe(CN)_6]^{3-/4-}$. The experiment was performed with three electrodes. Here, it is showed the result for just one electrode, since all of them showed similar trend. It was performed a CV measurement before the measurement in 20 mM TBA, with the first $[Fe(CN)_6]^{3-/4-}$ concentration and after the measurements in 20 mM TBA, in order to monitor variations of the conductivity. They are shown in Fig. 1B. The CV

measurement in 20 mM TBA and 0.1 mM $[Fe(CN)_6]^{3-/4}$ presented a second oxidative peak (in 0.22 V) when compared with the blank measurement (CV in 20 mM TBA). It was close to the oxidative peak of the $[Fe(CN)_6]^{3-/4}$ in 0.5 M KNO_3 and 12 mM PB, 0.25 V (Figure 26A), so it could represent the oxidation of the redox probe in solution. That difference in the oxidation potential could be due to the use of different supporting electrolyte. Also, the CV showed a decrease of the reduction peak, comparing with the reduction peak of the blank CV. After the measurement with the 6 solutions of TBA with $[Fe(CN)_6]^{3-/4}$, it was performed a measurement with TBA, in order to compare with the blank CV. It was observed a diminution of the conductivity of the system, maybe because of the destruction of the electroactive film.

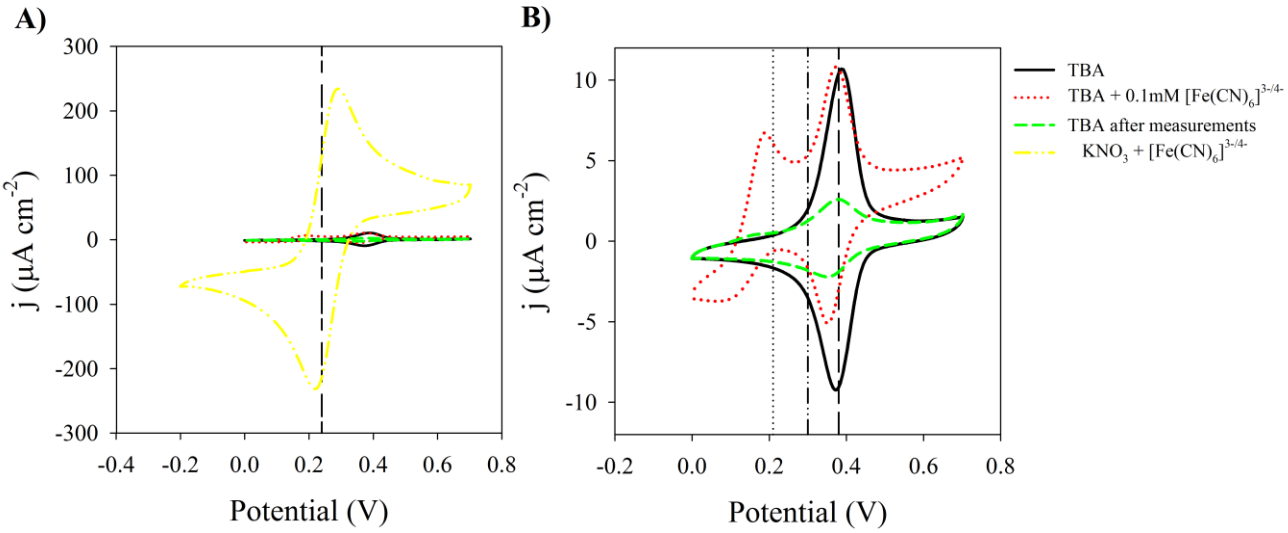

Figure 26 - Cyclic voltammetry plots of redox peptide SAM and redox probe in solution. A) CV in $[Fe(CN)_6]^{3-/4-}$ in 0.5 M KNO_3 and 12 mM PB, comparing to B) cyclic voltammetry of redox peptide-based SAM in 20 mM TBA; 20 mM TBA and 0.1 mM $[Fe(CN)_6]^{3-/4-}$; and in 20 mM TBA after the measurements. In A) vertical reference represents the formal potential of the $[Fe(CN)_6]^{3-/4-}$ in 0.5 M KNO_3 and 12 mM PB, 0.25 V (dotted line); in B) the vertical references show the formal potential of the confined redox probe (redox peptide SAM), 0.38 V *versus* Ag|AgCl 3M KCl (dashed line); of the redox probe in 20 mM TBA, 0.22 V *versus* Ag|AgCl 3M KCl (dotted line); and the half potential of both redox probe, 0.30 V *versus* Ag|AgCl 3M KCl (dash-dot line). Active gold electrode area: 0.045 cm^2.

Source: Author

As mentioned before, the EIS measurements were performed in three different potentials. The results are shown in Figure 27, Figure 28 and Figure 29, for each potential. When analysed in the formal potential of the electroactive SAM (0.38 V), it was observed a decrease of the capacitance of the system (Figure 27B, E and F), while the impedance kept almost invariable (Figure 27A, C, D). In the half-wave potential (0.30 V), the EIS measurements showed a lower variation of the capacitance of the system, but an increase of the diffusional region of

the measurements (Figure 28B, E and F); and a higher variation of the impedance (Figure 28A, C and D), comparing with those observed in the measurements in 0.38 V.

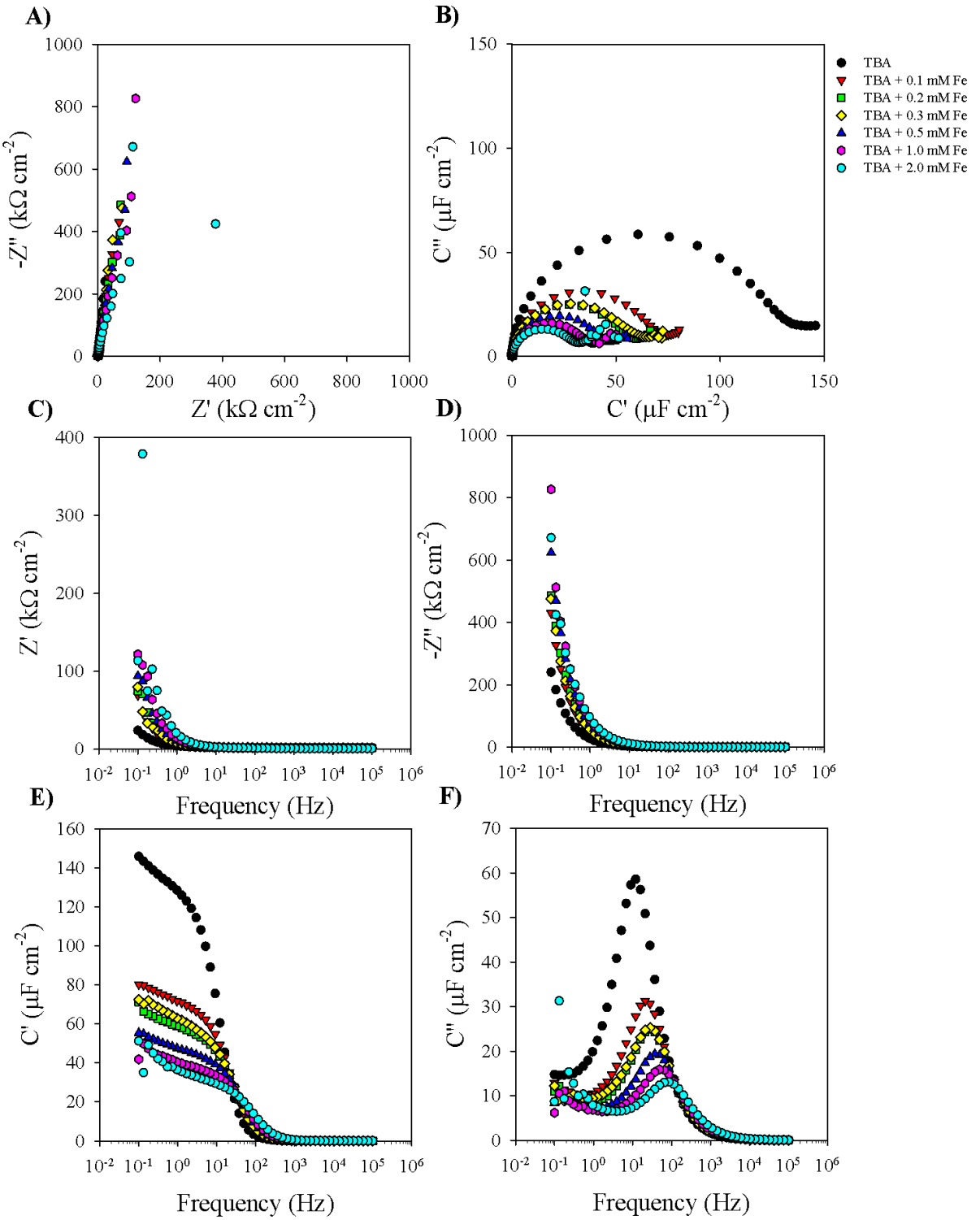

Figure 27 - EIS measurement in 0.38 V *versus* Ag|AgCl 3M KCl of the redox peptide SAM and redox probe in solution. A) Impedance Nyquist impedance plot; B) Capacitance Nyquist plot; C) Bode plot of real impedance (Z'); D) Bode plot of imaginary impedance (Z''); E) Bode plot of real capacitance (C'); F) Bode plot of imaginary capacitance (C''). Active gold electrode area: 0.045 cm^2.

Source: Author

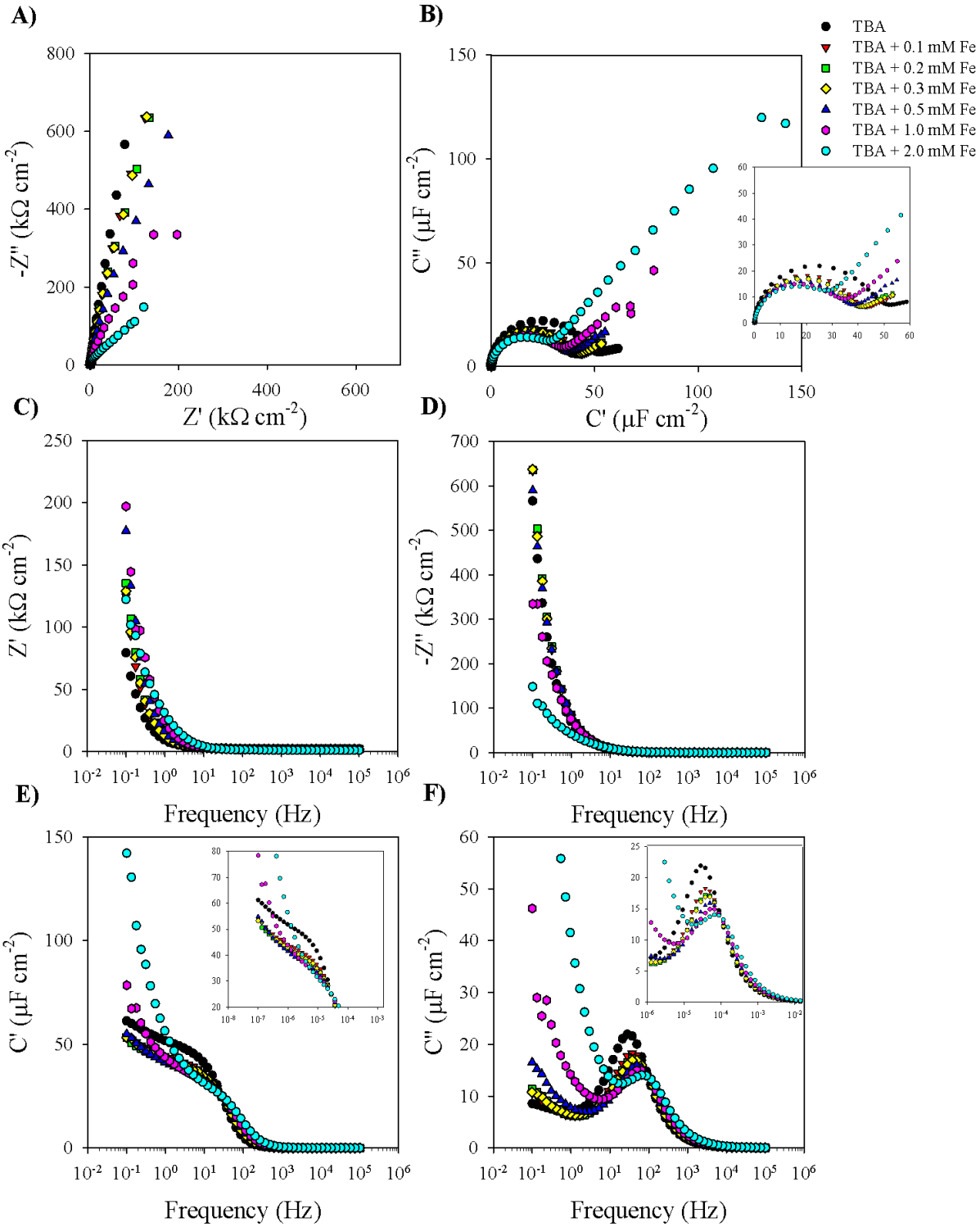

Figure 28 - EIS measurement in 0.30 V *versus* Ag|AgCl 3M KCl of the redox peptide SAM and redox probe in solution. A) Impedance Nyquist impedance plot; B) Capacitance Nyquist plot; C) Bode plot of real impedance (Z'); D) Bode plot of imaginary impedance (Z''); E) Bode plot of real capacitance (C'); F) Bode plot of imaginary capacitance (C''). Active gold electrode area: 0.045 cm^2.

Source: Author

Finally, the measurements at 0.38 V, showed a variation of the double layer capacitance (Figure 29B, E and F) and a diminution of the resistance of the system (Figure 29A, C and D).

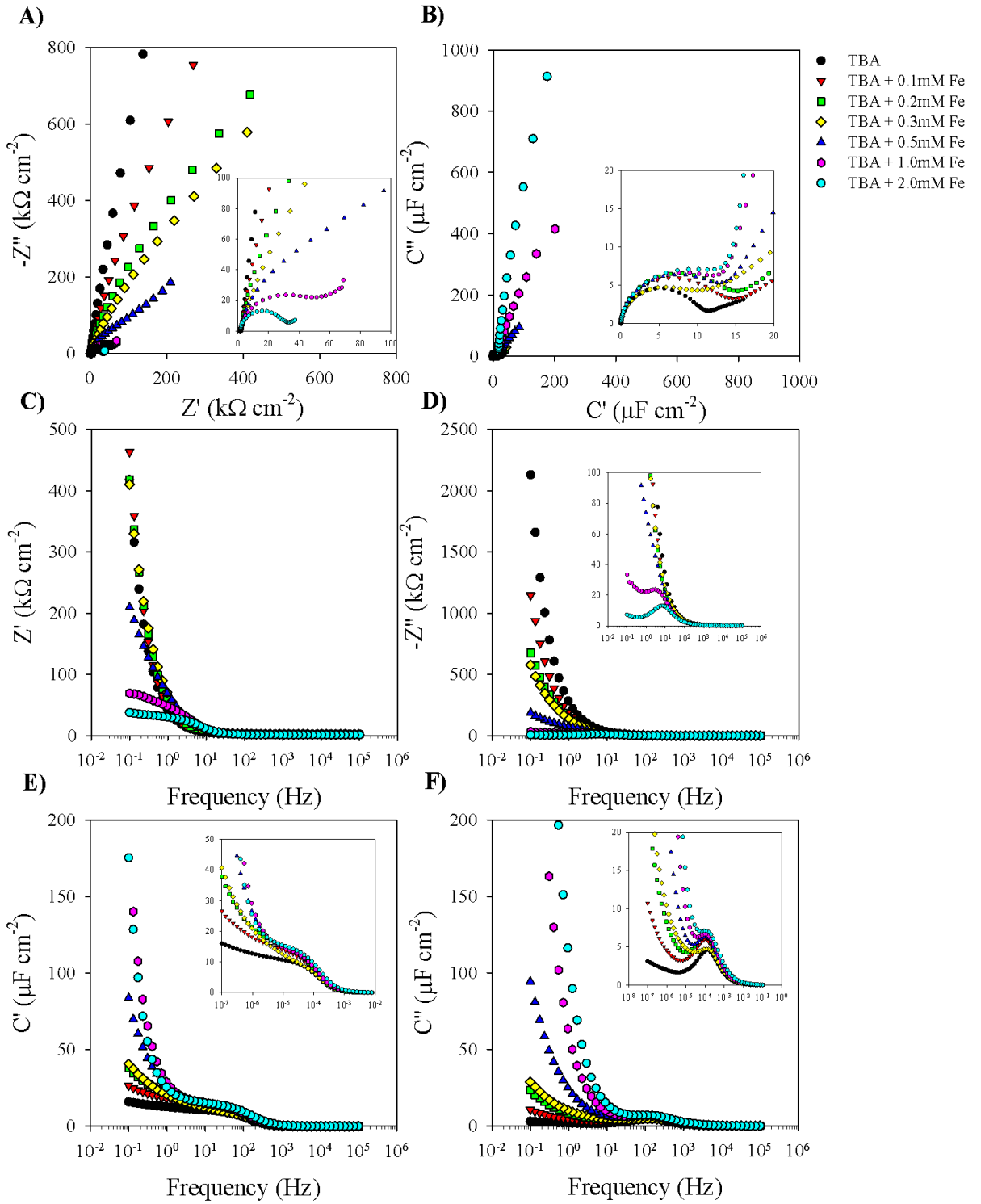

Figure 29 - EIS measurement in 0.22 V *versus* Ag|AgCl 3M KCl of the redox peptide SAM and redox probe in solution. A) Impedance Nyquist impedance plot; B) Capacitance Nyquist plot; C) Bode plot of real impedance (Z'); D) Bode plot of imaginary impedance (Z''); E) Bode plot of real capacitance (C'); F) Bode plot of imaginary capacitance (C''). Active gold electrode area: 0.045 cm^2.

Source: Author

This preliminary visual analysis was followed by a deeper analysis of the variables involved. It was studied the variation of the redox capacitive (C_r), the inverse of the redox capacitive ($1/C_r$), the frequency of charge relaxation (k), the system resistance (R_q), with the $[Fe(CN)_6]^{3-/4-}$ concentration increasing in each potential (Figure 30).

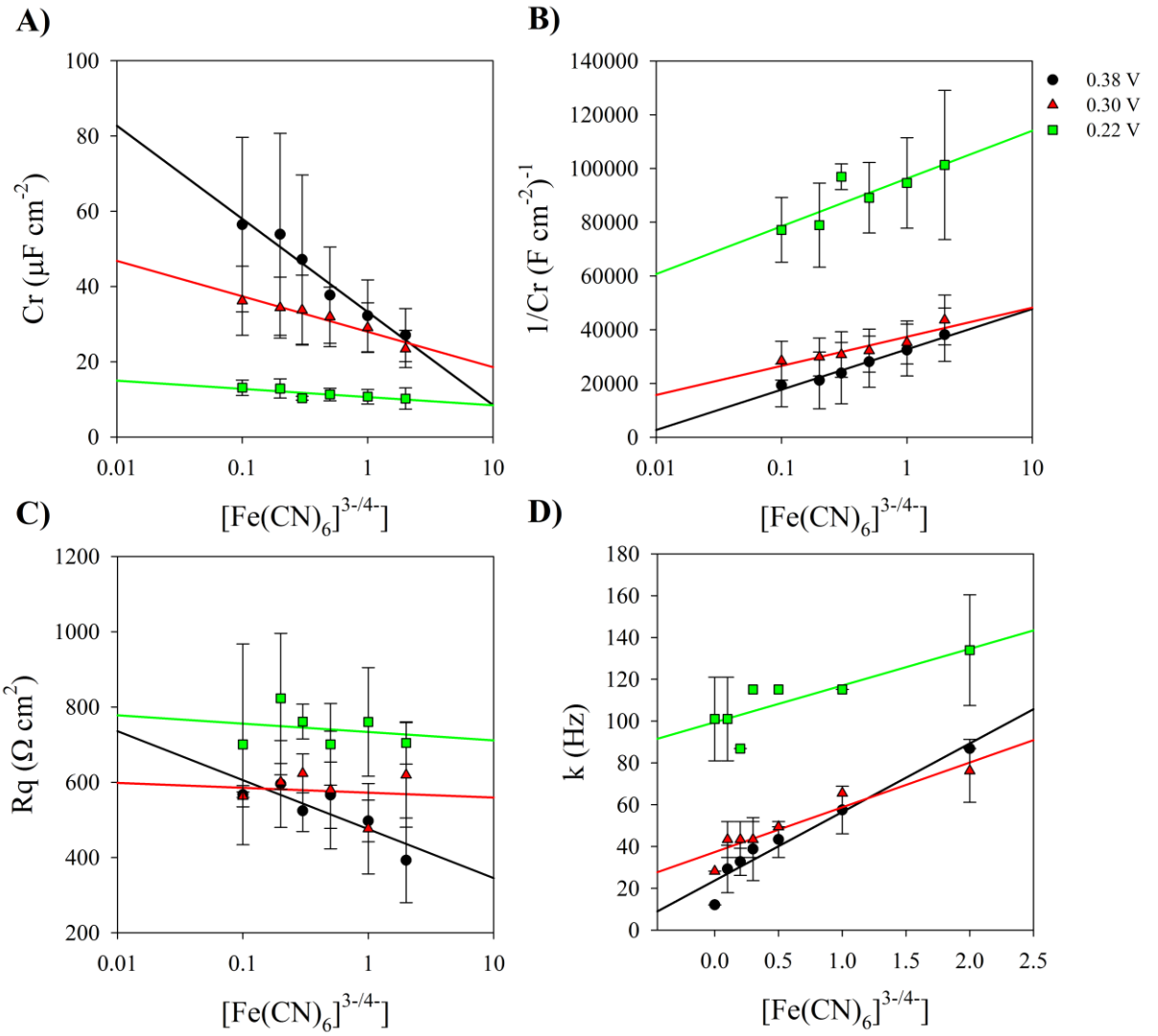

Figure 30 - Analysis of the variation of the variables involved on the charge transfer process of the system with both redox probe confined and in solution. A) Redox capacitance, C_r; B) Inverse of the redox capacitance, $1/C_r$; C) Resonance resistance, R_q; D) Frequency of charge relaxation, k. For each plot: black= EIS measurements in 0.38 V; red= EIS measurements in 0.30 V; green= EIS measurements in 0.22 V. The values were calculated with the results of two electrodes. The three electrodes showed the same trends, the variables varied similarly in the three electrodes in the presence of the redox probe in solution, however, the values was slightly different.

Source: Author

Table 5 - Correlation coefficients (r^2) of the lineal regression showed in Figure 29 for each variable and each potential.

Correlation coefficient (r^2)				
Potential	C_r	$1/C_r$	R_q	k
0.38 V	0.96*	0.98*	0.71	0.94*
0.30 V	0.93*	0.86*	0.01	0.89*
0.22 V	0.65	0.73	0.05	0.69

*Lineal correlations. Values with $r^2 > 0.85$ were considered as a lineal distribution.

The redox capacitance (Figure 30A) showed a higher diminution (80%) at the potential of the electroactive SAM (0.38 V) when increasing the concentration of the redox probe in solution, in comparison with the variation at the half-wave potential (54%). Redox capacitance is the variable used to monitor the surface variations in system based on ECS with electroactive films. It is related to the density-of-states of the redox probe confined at the surface. Hence, the system would be more sensitive to the presence of a second redox probe in the potential of the redox peptide-based SAM. As it is shown in Figure 27B, the capacitance of the system decreased when the concentration of the redox specie in solution increased, maybe because the electroactive film was losing electrons with the solution. Thus, the system was changing from a capacitance-based system to an impedance one. At the half-wave potential, the variation of the C_r value was lower, but it is important to highlight the changes in the Nyquist plot (Figure 28B). With the increasing of ferric/ferrous concentration in solution, the frequency of charge relaxation (k) increased and, so, the diffusion part of the Nyquist plot, showing the rise in the electrode-solution charge transfer. At the $[Fe(CN)_6]^{3-/4-}$ potential, C_r monitored the capacitance of the double layer (C_{dl}) or the dielectric capacitance (Figure 29B). It was almost imperceptible changes in its value and it did not present a lineal distribution (r^2 = 0.65), in contrast with the results at the potentials 0.38 V and 0.30 V (r^2 = 0.98 and 0.92, respectively) (Table 5). Thus, it was observed that the quantum capacitance (C_q) was more sensitive to the present of a second redox probe in solution and the variation in its concentration than the double layer capacitance (C_{dl}), which was almost invariable.

The inverse of the C_r was demonstrated to be proportional to the quantized energy (ΔE) of the system surface by Bueno, et al (2017). At the three potentials, ΔE increased with the concentration of redox probe in solution (Figure 30B). These variations would be in agreement with the expected results. In the measurements at 0.38 V, the energy storage in the system increased more than 300%, comparing between the values without redox probe in solution and with the highest concentration of it. At 0.30 V, the ΔE increased 120%; and at

0.22 V, 20%. This can be explained by the increase of the amount of redox species involved in the system. The redox species in solution contributed to the surface energy by the association with the redox probe confined. However, they did not contribute to the density of states of the electroactive film. The association between the confined redox probe and the redox probe in solution allowed to the charge transfer between the electroactive monolayer and the solution. After that, the charged redox probe in solution was diffused through the supporting electrolyte. Similar as the previous variables analysed, the results at 0.22 V did not showed a linear distribution, according to the r^2 of the regression (0.73; Table 5), so changes in the energy of the system could not be monitored at the potential of the redox probe in solution. $1/C_r$ at 0.22 V did not monitored the ΔE of the system, because C_r at 0.22 V did not monitor the redox capacitance of the system, but the C_{dl}.

The resonance resistance (R_q), wherein $R_q = R_T - R_s$, where R_s is the solution resistance; and R_T is the total resistance, calculated by $R_T = {}^{1}/_{C_r \cdot k}$. (Figure 30C) did not show a linear distribution at any of the potential tested. It was almost linear at the electroactive SAM potential (r^2=0.71). At the half-wave potential and at the ferric/ferrous potential it showed a random distribution. Here, we are going to considered a linear distribution the results obtained at 0.38 V and we are going to assume that the r^2<0.85 is due to experimental error. The resonance resistance of the system at 0.38 V decreased 30%, comparing without redox probe in solution and with the highest concentration of it. This result is in agreement with the observed for the rest of the variables studied. It was observed that the higher ferric/ferrous concentration, the higher electrode-solution charge transfer and the lower resistance. The presence of the redox probe in solution facilitated the electrode-solution charge transfer and so, the resonance resistant, because there were lower electrons in resonance between the electrode surface and the electroactive film.

Finally, it was analysed the frequency of charge relaxation (k). It also changed with the variation of the amount of electroactive specie in solution (Figure 30D). The variation was higher in the potentials 0.38 V and 0.30 V (r^2 = 0.96 and 0.86, respectively) than in 0.22 V, at which was not possible to observe a linear correlation. In both, 0.38 V and 0.30 V, the frequency of relaxation increased, and so the diffusional region of the Nyquist plots. Those results would be in agreement with the exposed previously for the C_r. The presence of the redox specie in solution changes the capacitive behaviour of the system and appeared an impedance contribution, due to the charge transfer between the electrode and the solution.

That increased the current density, which experimentally could be observed as a signal amplifier.

This preliminary study of the variables involved on the system allowed to observed and understand better the system with two redox probes (attached and in solution). It was observed the variation from a capacitive-based system to an impedance one with higher current density. Further experiments would be performed to understand better the advantages that the system could offer to very resistive system in terms of sensitivity.

5. Conclusion

A stable and quite reproducible impedimetric device was achieved. During the first part of the work, each step of the functionalization process was studied and evaluated. It was demonstrated the interaction between the antibody and the antigen by ELISA; the antibody immobilization on the modified electrode by QCM; and its orientation was controlled by protein A. However, not analytical response was achieved. The ferrocenylalkylthiol system from Lee and Lennox (LEE; LENNOX, 2007) suggested the presence of coverage defects (pinholes) on the thiolated monolayer. Those pinholes could be the reason of the absence of specific response. They would allow the redox couple to access freely the electrode surface, so the impedimetric phenomenon would not be effective. As a solution, ECS with an electroactive SAM was proposed, because the contributions of the non-faradaic processes (such as the SAM defects) to the system capacitance are lower than that due to the surface modifications, associated with the formal potential of the system. Nevertheless, it was not achieved an analytical response system for protein IL-6. Previous work based on ECS showed analytical curves for different proteins. This is the first time that ECS is used to detect the protein IL-6 and it is smaller than the protein already used previously by our group. Comparing the results of same ECS system (same SAM) used to detect different proteins, it was possible to correlate the molecular weight of the target and the receptor with the sensitivity of the system. According to that, the absence of response in the ECS system proposed here for IL-6 detection was associated to the molecular weight of the protein IL-6 (26 kDa). It was not considered big enough to be detected by the redox peptide based ECS system. Finally, it was studied the behaviour of a system with two redox probes (attached and in solution). It was observed the variation from a capacitive-based system, when only the confined redox probe was involved, to an impedance one, when the redox probe in solution was present. The presence of the two redox probes increased the current density and the energy of the system. The frequency of charge relaxation (k) increased with the increase of the redox probe in solution concentration and the redox capacitance (C_r) decreased. Those results showed that the two-redox probe configuration could be a signal amplifier system. It could be a good tool for high resistive systems and/or low sensitive systems.

In conclusion, the EIS and ECS electroanalytical techniques are widely used in biosensoring, since they show high sensitivity. However, they need an accurate control of the system design, in terms of the surface chemistry and the biosensoring interface, in order to achieved specific detection.

References

AMBLARD, M. et al. Methods and protocols of modern solid phase peptide synthesis. **Molecular Biotechnology**, v. 33, n. 3, p. 239–254, 2006.

ATKINSON, A. J. et al. Biomarkers and surrogate endpoints: Preferred definitions and conceptual framework. **Clinical Pharmacology and Therapeutics**, v. 69, n. 3, p. 89–95, 2001.

BAHADIR, E. B.; SEZGINTÜRK, M. K. A review on impedimetric biosensors. **Artificial Cells, Nanomedicine, and Biotechnology**, v. 44, n. 1, p. 248–262, 2016.

BARD, A. J.; FAULKNER, LARRY, R. **Electrochemical Methods:** Fundamentals and applications. 2nd. ed. New York: John Wiley & Sons, 2000.

BARTON, B. E. IL-6: Insights into novel biological activities. **Clinical Immunology and Immunopathology**, v. 85, n. 1, p. 16–20, 1997.

BOGOMOLOVA, A. et al. Challenges of electrochemical impedance spectroscopy in protein biosensing challenges of electrochemical impedance spectroscopy in protein biosensing. **Analytical Chemistry**, v. 81, n. 10, p. 3944–3949, 2009.

BOUBOUR, E.; LENNOX, R. B. Insulating properties of self-assembled monolayers monitored by impedance spectroscopy. **Langmuir**, v. 16, n. 9, p. 4222–4228, 2000.

BUENO, P. R.; FERNANDES, F. C. B.; DAVIS, J. J. Quantum capacitance as a reagentless molecular sensing element. **Nanoscale**, v. 9, p. 15362–15370, 2017.

CECCHETTO, J. et al. An impedimetric biosensor to test neat serum for dengue diagnosis. **Sensors and Actuators, B:** Chemical, v. 213, p. 150–154, 2015.

CECCHETTO, J. et al. The capacitive sensing of NS1 Flavivirus biomarker. **Biosensors and Bioelectronics**, v. 87, n. June 2016, p. 949–956, 2017.

CLARK, L. C.; LYONS, C. Electrode systems for continuous monitoring in cardiovascular surgery. **Annals Of The New York Academy Of Sciences**, v. 102, n. 1, p. 29–45, 1962.

DANIELS, J. S.; POURMAND, N. Label-free impedance biosensors: opportunities and challenges. **Electroanalysis**, v. 19, n. 12, p. 1239–1257, 2007.

FERNANDES, F. C. B. et al. Comparing label free electrochemical impedimetric and capacitive biosensing architectures. **Biosensors and Bioelectronics**, v. 57, p. 96–102, 2014.

FERNANDES, F. C. B. et al. Optimized diagnostic assays based on redox tagged bioreceptive interfaces. **Analytical Chemistry**, v. 87, n. 24, p. 12137–12144, 2015.

FERNANDES, F. C. B.; BUENO, P. R. Optimized electrochemical biosensor for human prostatic acid phosphatase. **Sensors and Actuators, B:** Chemical, v. 253, p. 1106–1112, 2017.

FISCHER, L. M. et al. Gold cleaning methods for electrochemical detection applications. **Microelectronic Engineering**, v. 86, n. 4–6, p. 1282–1285, 2009.

GUILBAULT, G. G.; MONTALVO, J. G. A urea-specific enzyme electrode. **Journal of the American Chemical Society**, v. 91, n. 8, p. 2164–2165, 1969.

HAMMOND, J. L. et al. Electrochemical biosensors and nanobiosensors. **Essays in Biochemistry**, v. 60, n. 1, p. 69–80, 2016.

HERMANSON, G. T. Bioconjugate Reagents. **Bioconjugate Techniques**, p. 214–233, 2008.

HORGAN, R. P.; KENNY, L. C. SAC review " Omic " technologies : proteomics and metabolomics. **The Obstetrician & Gynaecologist**, v. 13, p. 189–195, 2011.

KIECOLT-GLASER, J. et al. Chronic stress and age-related increases in the proinflammatory cytokine IL-6. **Proceedings of the National Academy of Sciences of the United States of America**, v. 100, n. 15, p. 9090–9095, 2003.

KONCKI, R. Recent developments in potentiometric biosensors for biomedical analysis. **Analytica Chimica Acta**, v. 599, n. 1, p. 7–15, 2007.

LANGONE, J. J. Protein A of Staphylococcus aureus and related immunoglobulin receptors produced by streptococci and pneumonococci. **Advances in Immunology**, v. 32, p. 157–252, 1982.

LEE, L. Y. S.; LENNOX, R. B. Ferrocenylalkylthiolate labeling of defects in alkylthiol self-assembled monolayers on gold. **Physical Chemistry Chemical Physics**, v. 9, n. 8, p. 1013–1020, 2007.

LEHR, J. et al. Mapping the ionic fingerprints of molecular monolayers. **Physical Chemistry Chemical Physics**, v. 19, n. 23, p. 15098–15109, 2017.

LISDAT, F.; SCHÄFER, D. The use of electrochemical impedance spectroscopy for biosensing. **Analytical and Bioanalytical Chemistry**, v. 391, n. 5, p. 1555–1567, 2008.

MACNAUGHT, A. D.; WILKINSON, A. **IUPAC. Compendium of Chemical Terminology, 2nd ed. (the "Gold Book")**. Disponível em: <https://goldbook.iupac.org/html/B/B00663.html>. Acesso em: 8 maio. 2017.

NUZZO, R. G.; ALLARA, D. L. Adsorption of bifunctional organic disulfides on gold surfaces. **Journal of the American Chemical Society**, v. 105, n. 13, p. 4481–4483, 1983.

ORAZEM, M. E.; TRIBOLLET, B. **Electrochemical Impedance Spectroscopy**. Hoboken, NJ, USA: John Wiley & Sons, 2008.

PICCOLI, J. et al. Redox capacitive assaying of C-reactive protein at a peptide supported aptamer interface. **Analytical Chemistry**, v. 90, n. 5, p. 3005–3008, 2018.

PICCOLI, J. P. et al. The self-assembly of redox active peptides: Synthesis and electrochemical capacitive behavior. **Biopolymers**, v. 106, n. 3, p. 357–367, 2016.

RAY, S.; MEHTA, G.; SRIVASTAVA, S. Label-free detection techniques for protein microarrays: Prospects, merits and challenges. **Proteomics**, v. 10, n. 4, p. 731–748, 2010.

SAENGER, W. Structure and dynamics of water surrounding biomolecules. **Annual Review of Biophysics and Biomolecular Structure**, v. 16, n. 1, p. 93–114, 1987.

SANTOS, A. et al. Redox-tagged peptide for capacitive diagnostic assays. **Biosensors and Bioelectronics**, v. 68, p. 281–287, 2015.

SANTOS, A.; BUENO, P. R.; DAVIS, J. J. A dual marker label free electrochemical assay for Flavivirus dengue diagnosis. **Biosensors and Bioelectronics**, v. 100, n. September 2017, p. 519–525, 2018.

SANTOS, A.; DAVIS, J. J.; BUENO, P. R. Fundamentals and applications of impedimetric and redox capacitive biosensors. **Journal of Analytical & Bioanalytical Techniques**, v. S7, n. 12, 2014.

SAUERBREY, G. Z. Z. Verwendung von schwingquarzen zur wägung dünner schichten und

zur mikrowägung. **Zeitschrift für Physik**, v. 115, p. 206–222, 1959.

SIGMA-ALDRICH. Molecular Self-Assembly. **Material Matters**, v. 1, n. 2, p. 1–19, 2006.

SIMÃO, E. P. et al. Biosensor based on cysteine monolayer and monoclonal antibody for specific detection of aflatoxin b1 in rice. **Journal of the Brazilian Chemical Society**, v. 27, n. 6, p. 1040–1047, 2016.

SMITH, R. K.; LEWIS, P. A.; WEISS, P. S. Patterning self-assembled monolayers. **Progress in Surface Science**, v. 75, n. 1–2, p. 1–68, 2004.

THERMO SCIENTIFIC. ELISA technical guide and protocols. **Thermo Scientific**, v. 65, n. 815, p. 1–14, 2010.

TRASATTI, S.; PETRII, O. A. Real surface area measurements in electrochemistry. **Pure and Applied Chemistry**, v. 63, n. 5, p. 711–734, 1991.

ULMAN, A. Formation and structure of self-assembled monolayers. **Chemical Reviews**, v. 96, n. 4, p. 1533–1554, 1996.

VERICAT, C.; VELA, M. E.; SALVAREZZA, R. C. Self-assembled monolayers of alkanethiols on Au(111): Surface structures, defects and dynamics. **Physical Chemistry Chemical Physics**, v. 7, n. 18, p. 3258, 2005.

VOGT, S. et al. Critical view on electrochemical impedance spectroscopy using the ferri/ferrocyanide redox couple at gold electrodes. **Analytical Chemistry**, v. 88, n. 8, p. 4383–4390, 2016.